Original scientific paper
https://doi.org/10.33180/InfMIDEM2026.201

Informacije MIDEM
Journal of Microelectronics, Electronic Components and Materials
Vol. 56, No. 2(2026), XX – XX

Interband Optical Absorption in Semiconductor Quantum Wells and Superlattices: A Unified Effective-Mass Analysis of Confinement, Tunneling, and Miniband Dispersion

Nasirov Mardonbek Khaldarbekovich[a,b]*, Sulaymonov Khusanboy Mannopovich[a], Umarov Abdusattor Ortiqovich[a], Rakhmonov Tokhirbek Imomaliyevich[a], Karimov Sherali Xasanovich[b], Mirsodikov Abdulla Tursunalievich[b], Axmadjanova Shaxnoza Shakirovna[a], Rasulov Voxob Rustamovich[b]

[a]*Fergana State Technical University, Fergana, Uzbekistan*
[b]*Fergana State University, Fergana, Uzbekistan*

Correspondence to:
Nasirov Mardonbek Xaldarbekovich
Physics Department, Fergana State Technical University, Fergana, Uzbekistan
E-mail: nasirovmardonbek92@gmail.com

Abstract.

A unified theoretical framework for interband optical absorption in semiconductor quantum wells and periodic superlattices is developed within the effective-mass approximation and the envelope-wave-function formalism. Carrier states are obtained for isolated quantum wells with infinite and finite barriers and extended to periodic superlattices using transfer-matrix and Bloch analyses. Analytical expressions are derived for the optical transition probability, optical joint density of states, and absorption coefficient, and numerical calculations are performed for an InAs/InAsSb type-II superlattice using experimentally reported structural parameters. The calculations reproduce the transition from the blue-shifted, step-like absorption of isolated quantum wells to the broadened near-edge response of superlattices governed by miniband dispersion and the electron–heavy-hole envelope-function overlap. The calculated ground-state transition threshold and absorption coefficient show reasonable agreement with published room-temperature measurements, supporting the applicability of the proposed framework to infrared semiconductor heterostructures.

Keywords: interband optical absorption; semiconductor quantum wells; semiconductor superlattices; quantum confinement; miniband dispersion; effective-mass approximation; optical density of states; semiconductor heterostructures

Medpasovna optična absorpcija v polprevodniških kvantnih jamah in supermrežah:

Enotna analiza efektivne mase z vidika omejitve, tuneliranja in disperzije mini pasov

Izvleček

V okviru aproksimacije efektivne mase in formalizma ovojne valovne funkcije je razvit enoten teoretični okvir za medpasovno optično absorpcijo v polprevodniških kvantnih jamah in periodičnih supermrežah. Stanja nosilcev so določena za izolirane kvantne jame z neskončnimi in končnimi pregradami ter razširjena na periodične supermreže z uporabo analize prenosne matrike in Blochove analize. Izpeljani so analitični izrazi za verjetnost optičnega prehoda, skupno gostoto optičnih stanj in absorpcijski koeficient, izvedeni pa so tudi numerični izračuni za supermrežo tipa II InAs/InAsSb z uporabo eksperimentalno poročanih strukturnih parametrov. Izračuni ponazarjajo prehod od modro pomaknjene, stopničaste absorpcije izoliranih kvantnih jam do razširjenega odziva supermrež v bližini roba, ki ga določata disperzija minibandov in prekrivanje ovojnih funkcij elektronov in težkih lukenj. Izračunani prag prehoda v osnovnem stanju in absorpcijski koeficient se razumno ujemata z objavljenimi meritvami pri sobni temperaturi, kar podpira uporabnost predlaganega okvira za infrardeče polprevodniške heterostrukture.

Ključne besede: medpasovna optična absorpcija; polprevodniške kvantne jame; polprevodniške supermreže; kvantno omejevanje; minipasovna disperzija; aproksimacija efektivne mase; optična gostota stanj; polprevodniške heterostrukture

1. Introduction.

Low-dimensional semiconductor heterostructures such as quantum wells and superlattices have attracted sustained interest because their electronic and optical properties can be tailored through nanoscale structural design. When semiconductor layers with different band gaps and band offsets are combined, carriers become confined along the growth direction while remaining nearly free in the plane of the layers. This reduced dimensionality modifies the carrier spectrum, transforms the density of states, and strongly affects the threshold behavior and line shape of interband optical absorption. As a result, quantum-confined heterostructures provide a versatile platform for the development of spectrally selective photodetectors, optical modulators, absorbers, and other optoelectronic devices. Related ZnO/Si heterojunction solar-cell studies further highlight that band alignment, interface quality, and carrier-transport control are critical parameters governing the photovoltaic and optoelectronic performance of semiconductor heterostructures [1]. The relevance of quantum-well absorption engineering to optical modulation has been demonstrated in strained quantum-well structures, where theoretical and experimental analyses linked confinement and strain effects to the absorption response [2]. Such confinement-engineered absorption is directly relevant to multiple-quantum-well optoelectronic structures, including GaNAsBi-based MQWs designed for optical response near the telecommunication wavelength of 1.55 μm [3].

In isolated quantum wells, size quantization produces discrete electron and hole subbands and a two-dimensional optical density of states. In periodic superlattices, finite-barrier tunneling couples equivalent states in neighboring wells and transforms the discrete levels into dispersive minibands. A consistent comparison of these regimes is required to distinguish the respective roles of confinement, barrier penetration, and interwell coupling in determining the absorption spectrum.

Although quantum wells and superlattices have been extensively studied, a compact treatment that compares both systems within the same analytical and numerical framework remains useful. Such a

formulation should distinguish the contributions of quantum confinement, finite-barrier penetration, miniband dispersion, and envelope-function overlap to the measured optical response.

In this work, carrier states are derived for isolated quantum wells with infinite and finite barriers and for periodic superlattices described by transfer-matrix and Bloch methods. These states are used to formulate the optical transition probability, optical joint density of states, and interband absorption coefficient. The numerical analysis is performed for an InAs/InAsSb type-II superlattice using experimentally reported structural and band-edge parameters.

The contribution of the present work is the use of a common effective-mass formalism to connect isolated-well confinement, finite-barrier tunneling, superlattice miniband dispersion, and interband absorption. In addition to the analytical comparison, the model is evaluated through a $\boldsymbol{q}$-resolved calculation of the transition energy and electron–heavy-hole overlap for an experimentally characterized InAs/InAsSb type-II superlattice.

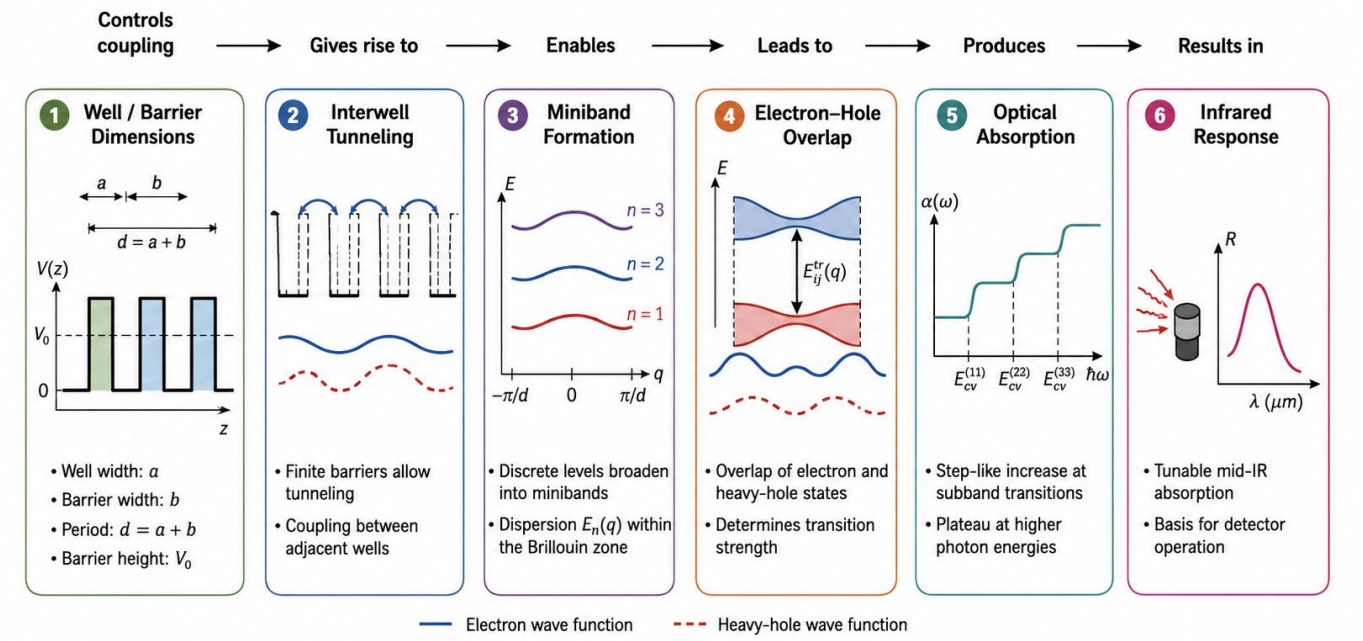

Figure 1. Structure–optical-response pathway in a semiconductor superlattice. The well width $\boldsymbol{a}$, barrier width $\boldsymbol{b}$, superlattice period $\boldsymbol{d = a + b}$, and barrier height $\boldsymbol{V_0}$ determine interwell tunneling and miniband formation. The resulting $\boldsymbol{q}$-dependent electron and heavy-hole states control their envelope-function overlap and interband optical-transition strength, thereby determining the absorption coefficient and infrared spectral response of the superlattice.

2. Physical Model and Basic Assumptions.

The systems considered in this work are low-dimensional semiconductor heterostructures formed by alternating semiconductor layers with different band-gap energies, which produce band alignment and corresponding conduction- and valence-band offsets at the interfaces [4]. An isolated quantum well is treated as a one-dimensional confinement potential along the growth direction, whereas a superlattice is represented by a periodic arrangement of quantum wells and barriers with structural period $\boldsymbol{d = a + b}$, where $\boldsymbol{a}$ and $\boldsymbol{b}$ denote the well and barrier widths, respectively [5]. This idealized superlattice model is directly connected to experimentally realized type-II superlattice absorbers. For instance, Webster et al. studied MBE-grown InAs/InAsSb superlattices on GaSb substrates and extracted their absorption coefficients using room-temperature spectroscopic ellipsometry. The periodic InAs/InAsSb layer sequence in their structures serves as a practical experimental realization of the alternating well–barrier potential considered in the present work. This correspondence indicates that the periodic potential approximation used here provides a physically relevant basis for interpreting the optical absorption response of real type-II superlattice heterostructures. Because the heterostructure is translationally invariant in the layer plane, carrier motion is treated as free in the in-plane directions and quantized only along the growth direction. This quasi-two-dimensional description captures the confinement-induced modification of the carrier spectrum that governs interband optical absorption. As schematically shown in Fig. 2(a), confinement along

the z direction produces discrete subband levels, whereas Fig. 2(b) illustrates the parabolic in-plane dispersion associated with free carrier motion in the layer plane [6–8].

The confining potentials for electrons and holes arise from the discontinuities of the conduction- and valence-band edges at the heterointerfaces. The active layer, characterized by a smaller band gap, forms a potential well, whereas the surrounding wider-gap layers act as barriers. For the type-II InAs/InAsSb superlattice considered in the numerical analysis, the electron and heavy-hole confinement potentials are distinct: electrons are localized predominantly in the InAs-rich layers, whereas heavy holes are confined mainly in the Sb-rich InAsSb layers. In an isolated quantum well, this confinement leads to discrete size-quantized subbands. In a periodic superlattice, however, tunneling through the barriers couples neighboring wells and causes these discrete levels to broaden into minibands. The distinction between discrete subbands and dispersive minibands is central to the present study, since it governs the threshold behavior and spectral shape of interband optical absorption.

The theoretical treatment is based on the effective-mass approximation and the envelope-wave-function formalism. Within this approach, the carrier states near the relevant band extrema are described by slowly varying envelope functions multiplying the corresponding Bloch states. The approximation is valid when the characteristic confinement length is sufficiently larger than the lattice constant, allowing the microscopic crystal potential to be represented through material-dependent effective masses and band offsets. The theoretical justification of the effective-mass approximation in semiconductor microstructures supports its use when the envelope function varies slowly on the scale of the lattice constant [9]. As a consequence, the heterostructure problem is reduced to solving one-dimensional envelope-function equations with piecewise-defined parameters in the growth direction.

For analytical transparency, the present model is formulated within the single-particle approximation. Electron-hole Coulomb interaction, excitonic effects, many-body renormalization, and carrier scattering processes are not included explicitly. Furthermore, the interfaces are assumed to be abrupt and ideal, while interface roughness, alloy disorder, impurity effects, internal electric fields, and strain-induced perturbations are neglected. Under these assumptions, the calculated absorption characteristics represent the intrinsic confinement-driven optical response of idealized quantum-well and superlattice structures.

This model provides a unified framework for describing both isolated and periodically coupled heterostructures. In particular, it enables the roles of structural confinement, barrier penetration, and interwell tunneling to be analyzed consistently in relation to the absorption edge, the optical density of states, and the resulting spectral line shape. Such a formulation is especially useful for identifying the physical origin of step-like absorption in quantum wells and its gradual smoothing in superlattices due to miniband dispersion.

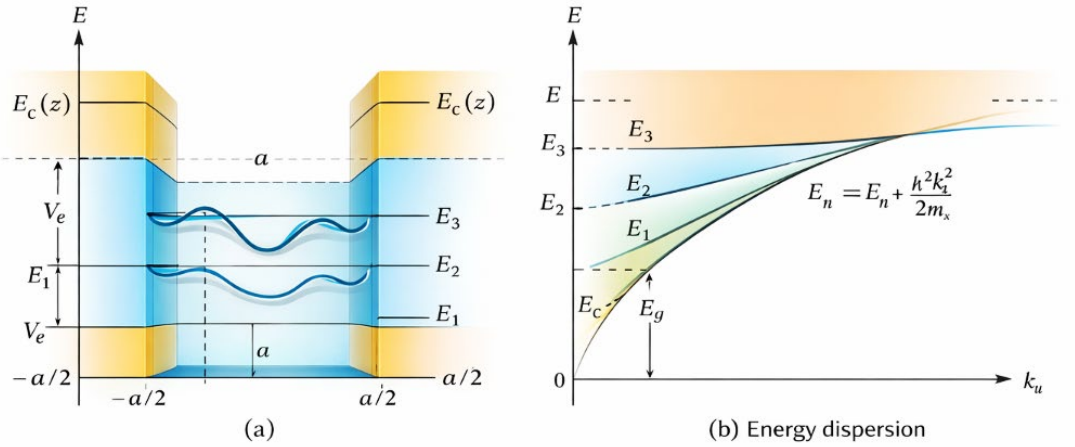

Figure 2. Schematic illustration of carrier confinement and energy dispersion in a semiconductor quantum well. (a) One-dimensional band-edge profile along the growth direction z, showing the conduction band $E_c(z)$ and valence band offsets that form a finite potential well of width (a). Quantum confinement leads to the formation of discrete electron subband levels E_1, E_2, and E_3, with corresponding envelope wave functions localized within the well and partially penetrating into the barrier regions. (b) In-plane energy

dispersion of the quantized subbands, illustrating the quasi-two-dimensional nature of carrier motion. While carriers are confined along the growth direction, they remain free in the (x)–(y) plane, resulting in parabolic subband dispersions described by $E_n(k_\parallel) = E_n + \frac{\hbar^2 k_\parallel^2}{2m^*}$. The band gap E_g and subband separation determine the threshold energies for interband optical transitions.

The schematic potential profiles introduced above form the basis for the carrier-state analysis presented in the following section. As shown schematically in Fig. 3(a), a semiconductor superlattice is formed by a periodic sequence of quantum wells and barriers, producing a one-dimensional confinement potential with period $\boldsymbol{d = a + b}$. In contrast to an isolated quantum well, where the carrier spectrum consists of discrete size-quantized levels, the finite barrier transparency in a periodic structure enables tunneling between neighboring wells. As a result, the corresponding confined states are no longer strictly localized, but broaden into minibands, as illustrated in Fig. 3(b). This miniband formation introduces an additional dispersion of the carrier energy along the superlattice axis and plays a key role in determining the near-edge interband optical absorption spectrum.

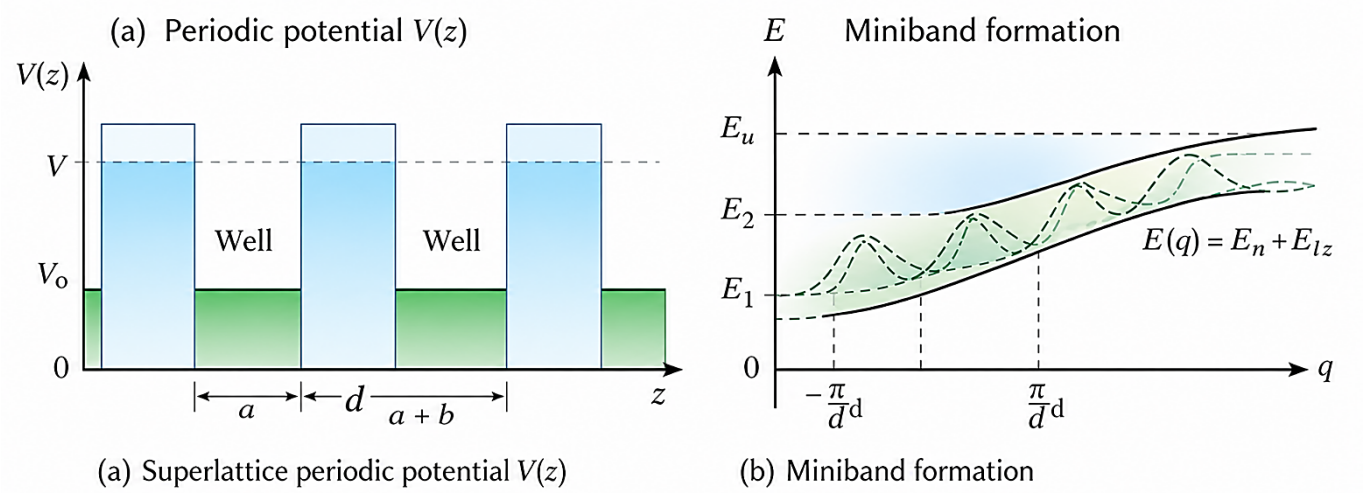

Figure 3. Schematic illustration of miniband formation in a semiconductor superlattice. (a) Periodic potential profile $V(z)$ formed by alternating quantum wells and barriers with period $d = a + b$. (b) Discrete confined levels of an isolated well broaden into minibands due to interwell tunneling, giving rise to energy dispersion along the superlattice axis.

For clarity and consistency, the following notation is adopted throughout this work. The growth direction is taken along the z axis, whereas $\rho = (x, y)$ denotes the in-plane coordinate. The in-plane carrier wave vector is denoted by $k_\parallel$, while q is used for the Bloch wave vector along the superlattice direction. The widths of the quantum well and barrier are denoted by a and b, respectively, and the superlattice period is defined as $d = a + b$. The effective masses of carriers in the well and barrier regions are written as m_A and m_B, respectively. The confinement energies of the electron and hole subbands are denoted by $E_{e,i}$ and $E_{h,j}$, while E_g represents the band gap of the well material. Unless explicitly stated otherwise, the theoretical treatment is developed within the single-particle effective-mass approximation and the envelope-function formalism.

3. Carrier States in Isolated Quantum Wells.

Within the effective-mass approximation, the carrier states in an isolated quantum well are obtained by solving the one-dimensional Schrödinger equation along the growth direction. We first consider the limiting case of an infinitely deep quantum well, which provides a useful reference for understanding the effect of finite barrier height and interwell coupling in superlattices.

$$\Psi_{n,k_\parallel}(r)\frac{1}{\sqrt{S}}exp(ik_\parallel \cdot \rho)\phi_n(z), \quad (1)$$

where $r = (\rho, z)$), $\rho = (x, y)$ denotes the in-plane coordinate, $k_{\parallel}$ is the corresponding in-plane wave vector, and $\phi_n(z)$ is the envelope wave function associated with the n- size-quantized subband. In a $B/A/B$ -type structure, $\varphi(z)$

$$\left[-\frac{\hbar^2}{2m_A}, \frac{d^2}{dz^2} + V(z)\right]\phi_n(z) = E_n, \phi_n(z),$$

$$\mathrm{V(z)} = \begin{cases} 0 & |\mathrm{z}| < \mathrm{a}/2, \\ \infty & |\mathrm{z}| \geq \mathrm{a}/2. \end{cases} \tag{2}$$

The solution to the one-dimensional Schrödinger equation can be written in the following form, where m_A is the effective mass of the particle in layer A of the structure. Outside layer A, the function $\varphi(z)$ vanishes. The total energy of the particle, E, is composed of the sum of the one-dimensionally quantized energy E_z and the kinetic energy $E_{xy} = \hbar^2 q^2 / 2m_A$. When the origin of coordinates is placed at the center of the well, the potential symmetry causes the eigenfunctions to separate into even and odd solutions. Therefore, the electron wave functions may be represented by two types of states, namely even and odd wave functions, which can be chosen in the forms $C\cos(kz)$ and $C\sin(kz)$, respectively. Here, $k = (2m_A E_z/\hbar^2)^{1/2}$, and S is the normalization coefficient. From the boundary conditions, the allowed wave numbers and the corresponding confinement energies along the growth direction are obtained as:

$$k_n = \frac{n\pi}{a}, \qquad E_n^{(z)} = \frac{\hbar^2 k_n^2}{2m_A} = \frac{\hbar^2}{2m_A}\left(\frac{n\pi}{a}\right)^2, \qquad n = 1,2,3, \ldots \tag{3}$$

The corresponding eigenstates may be classified according to their spatial parity with respect to the center of the well: odd values of $\boldsymbol{n}$ correspond to even-parity states, whereas even values of $\boldsymbol{n}$ correspond to odd-parity states. The total carrier energy is the sum of the confinement energy along the growth direction and the free-carrier kinetic energy in the layer plane. Therefore,

$$E_n(k_{\parallel}) = E_n^{(z)} + \frac{\hbar^2 k_{\parallel}^2}{2m_A} = \frac{\hbar^2}{2m_A}\left[\left(\frac{n\pi}{a}\right)^2 + k_{\parallel}^2\right] \tag{4}$$

Here, $\boldsymbol{k_{\parallel}} = |\boldsymbol{k_{\parallel}}|$ is the magnitude of the in-plane carrier wave vector. Equation (4) describes a set of quasi-two-dimensional size-quantized subbands with parabolic in-plane dispersion. At the subband edge, where $\boldsymbol{k_{\parallel}} = 0$, the total carrier energy reduces to the confinement energy $\boldsymbol{E_n^{(z)}}$. For a finite-height potential barrier, the envelope wave function penetrates into layer $\boldsymbol{B}$ and remains nonzero in the barrier region. The corresponding equation in layer $\boldsymbol{B}$ can be written as follows:

$$\left(-\frac{\hbar^2}{2m_B}\frac{d^2}{dz^2} + V\right)\varphi(z) = E_z\varphi(z).$$

This is the solution of the stationary Schrödinger equation of the form given above. Here, V is the potential barrier, representing the energy offset between the conduction-band edges at the interface. For the finite potential well, the envelope function must satisfy the standard BenDaniel–Duke (Bastard-type) boundary conditions at the heterointerface, which ensure the continuity of the wave function and the probability current across the interface.

$$\phi_A = \phi_B, \qquad \frac{1}{m_A}\frac{d\phi}{dz}\bigg|_A = \frac{1}{m_B}\frac{d\phi}{dz}\bigg|_B \tag{5}$$

Here, m_A and m_B are the carrier effective masses in the well and barrier regions, respectively. These boundary conditions are adopted throughout the present analysis of finite quantum wells and superlattices. These conditions correspond to the BenDaniel–Duke boundary conditions, which ensure continuity of the envelope function and probability current across heterointerfaces with different effective masses [10].

For a quantum well with finite barrier height $\boldsymbol{V_0}$, the envelope function remains oscillatory inside the well and decays exponentially in the barrier regions. Accordingly, the solution may be written in the form

$$\varphi(\mathrm{z}) = \begin{cases} C_e\, cos(k\, z), & |z| \leq \frac{a}{2}, \\ D_e\, exp\left[-\kappa\left(|z| - \frac{a}{2}\right)\right], & |z| \geq \frac{a}{2}. \end{cases} \tag{6}$$

$$\varphi(z) = \begin{cases} C_o \sin(k\,z), & |z| \le \frac{a}{2}, \\ D_o\, sgn(z) exp\left[-\kappa\left(|z| - \frac{a}{2}\right)\right] & |z| > \frac{a}{2}. \end{cases}$$

Here, $\boldsymbol{sgn(z) = +1}$ for $\boldsymbol{z > 0}$ and $\boldsymbol{sgn(z) = -1}$ for $\boldsymbol{z < 0}$. This factor ensures the odd-parity condition $\phi_o(-z) = -\phi_o(z)$ in both barrier regions. Here, $k = [2m_A(E_n)/\hbar^2]^{\frac{1}{2}}$, $\kappa = [2m_B(V - E_z)/\hbar^2]^{\frac{1}{2}}$, where the size-quantization energy levels are assumed to be smaller than the potential-well height, and the wave vector in the barrier layer is taken to be imaginary, $k_B = i\kappa$. Taking relation (6) into account, the following result is obtained from the system of equations in the form of Eq. (5): Applying the boundary conditions at $\boldsymbol{z = a/2}$ to the even-parity solution yields

$$C\cos\left(\frac{ka}{2}\right) = D, \qquad \frac{k}{m_A} C \sin\left(\frac{ka}{2}\right) = \frac{\kappa}{m_B} D \tag{7}$$

Eliminating the coefficients $\boldsymbol{C}$ and $\boldsymbol{D}$ from Eq. (7) leads to the transcendental equation that determines the allowed energy levels of the even states

$$\tan\left(\frac{ka}{2}\right) = \eta = \frac{m_A \kappa}{m_B k} \tag{8}$$

whereas the energy spectrum of the odd states is given by

$$\cot\left(\frac{ka}{2}\right) = -\eta \tag{9}$$

is determined by means of a transcendental equation of the above form. For bound states in a finite quantum well, the wave vector inside the well and the decay constant in the barrier region are defined as

$$k = \left(\frac{2m_A E_z}{\hbar^2}\right)^{1/2}, \qquad \kappa = \left[\frac{2m_B(V_0 - E_z)}{\hbar^2}\right]^{1/2} \tag{10}$$

Here, k characterizes the oscillatory behavior of the envelope function in the well region, whereas κ describes its exponential decay inside the barrier. Thus, in a finite-height potential well, the spectrum consists of a finite number of quantized levels and continuum states at higher energies. In the limit of a high barrier height, the finite-well model approaches the result for an infinitely deep well; in this case, the ground-state energy can be expressed by the following approximation. For this purpose, the potential-well height V is taken as

$$V \gg \frac{\hbar^2}{2m_A}\left(\frac{\pi}{a}\right)^2 \tag{11}$$

Under the high-barrier condition specified in Eq. (11), the barrier decay constant for the ground state may be approximated by $\kappa \approx \kappa_0 = \frac{\sqrt{2m_B V_0}}{\hbar}$. The ground state has even parity. Its wave number can therefore be written as a small correction to the infinite-well value: $k = \frac{\pi}{a} - \delta k,\ \delta k\, a \ll 1$. Taking the reciprocal of the even-state quantization condition in Eq. (8) gives $\cot\left(\frac{ka}{2}\right) = \frac{m_B k}{m_A \kappa}$. Using $\frac{ka}{2} = \frac{\pi}{2} - \frac{\delta k\, a}{2}$, the left-hand side becomes $\cot\left(\frac{ka}{2}\right) = \tan\left(\frac{\delta k\, a}{2}\right) \approx \frac{\delta k\, a}{2}$, where the small-argument approximation $\tan x \approx x$ has been used. Replacing k and κ on the right-hand side by their zeroth-order values π/a and κ_0, respectively, gives $\frac{\delta k\, a}{2} \approx \frac{m_B}{m_A}\frac{\pi}{\kappa_0 a}$. Consequently, the ground-state wave number in the first-order approximation is $k \approx \frac{\pi}{a}\left(1 - \frac{2m_B}{m_A \kappa_0 a}\right)$. Substituting this expression into $E_1 = \hbar^2 k^2/(2m_A)$ and retaining only terms of first order in $1/(\kappa_0 a)$, the ground-state energy becomes. In the high-barrier limit, the ground-state energy of the finite quantum well can be approximated by

$$E_1 \approx \frac{\hbar^2}{2m_A}\left(\frac{\pi}{a}\right)^2\left(1 - \frac{4m_B}{m_A \kappa_0 a}\right), \qquad \kappa_0 = \sqrt{\frac{2m_B V_0}{\hbar^2}} \tag{12}$$

This expression shows that the ground-state energy in a finite well is slightly reduced compared with the infinite-well result because of wave-function penetration into the barrier region.

4. Tunneling-Induced Miniband Dispersion in Periodic Superlattices.

The effective mass approximation and the envelope-function method constitute one of the most convenient approaches for describing the spectrum of charge carriers in quantum wells and superlattices. Within this framework, the effective mass of charge carriers in each layer is taken to depend on the bulk crystal parameters, and the energy spectrum is determined by solving the envelope-function equations. Within the effective-mass approximation, the carrier states in a periodic quantum-well superlattice are described by the envelope-function equation, The envelope-function approximation has been widely used for calculating superlattice band structures and provides a suitable theoretical basis for describing miniband formation in periodically coupled quantum wells [11].

$$\left[-\frac{\hbar^2}{2m_{\parallel}}\nabla_{\parallel}^2-\frac{\hbar^2}{2m_z}\frac{d^2}{dz^2}+V(z)\right]F(r)=E\,F(r) \tag{13}$$

Here $m_{\parallel}$, and m_z are the effective masses associated with carrier motion parallel and perpendicular to the layers, respectively, $V(z)$ is the periodic confinement potential along the growth direction, and $F(r)$ is the envelope wave function. Because the structure is translationally invariant in the plane of the layers, the envelope function can be separated into an in-plane plane-wave part and a confinement-dependent part along the growth direction as

$$F(r)=e^{ik_{\parallel}\cdot\rho}\,\phi(z) \tag{14}$$

Here, $\boldsymbol{\rho}=(\boldsymbol{x},\boldsymbol{y})$ denotes the in-plane coordinate, $\boldsymbol{k}_{\parallel}$ is the corresponding in-plane wave vector, and $\boldsymbol{\phi}(\boldsymbol{z})$ describes the carrier confinement along the growth direction. Substitution of Eq. (14) into Eq. (13) reduces the three-dimensional envelope-function equation to an effective one-dimensional problem along the growth axis.

For an infinitely deep quantum well, the confinement potential produces discrete envelope states with definite spatial parity with respect to the center of the well. The normalized eigenfunctions can therefore be written as:

$$\phi_n(z)=\begin{matrix}\sqrt{\frac{2}{a}}\cos\left(\frac{n\pi z}{a}\right),n=1,3,5,\dots,\\ \sqrt{\frac{2}{a}}\sin\left(\frac{n\pi z}{a}\right),n=2,4,6,\dots,\end{matrix} \tag{15}$$

Odd values of n correspond to even-parity states, whereas even values of n correspond to odd-parity states. These localized well states provide the basis for describing miniband formation when neighboring wells are coupled through finite barriers. A detailed theoretical treatment of superlattice band formation shows that coupling between localized quantum-well states through finite barriers leads to dispersive minibands whose widths are controlled by the barrier parameters [12]. The corresponding confinement energies are given by Eq. (3). For a carrier state characterized by the in-plane wave vector $\boldsymbol{k}_{\parallel}=(\boldsymbol{k_x},\boldsymbol{k_y})$, the total energy can be decomposed into an in-plane kinetic contribution and a confinement-related contribution along the growth direction. Accordingly, the wave number in the well region is written as

$$k^2=\frac{2m_z}{\hbar^2}(E-E_{\parallel}),\qquad E_{\parallel}=\frac{\hbar^2k_x^2}{2m_{\parallel}}+\frac{\hbar^2k_y^2}{2m_{\parallel}} \tag{16}$$

Here, $E_{\parallel}$ is the in-plane kinetic energy associated with free carrier motion parallel to the layers, while k determines the oscillatory behavior of the envelope function in the well region. This decomposition is useful for connecting the confined well states to the miniband description of the periodic superlattice. In the idealized limit of an infinitely deep rectangular quantum well, the confinement potential is represented by

$$\mathrm{V(z)}=\begin{cases}0, & |\mathrm{z}|<\mathrm{a}/2,\\ \infty, & |\mathrm{z}|\geq\mathrm{a}/2.\end{cases} \tag{17}$$

Under this assumption, the envelope function vanishes outside the well region, and the confined states are fully determined by the boundary conditions at $z=\pm a/2$. This limiting case is useful as a reference for understanding the modification of the spectrum when finite barriers and interwell coupling are introduced.

For a more realistic description of coupled quantum-well systems, the infinite-barrier approximation must be relaxed by introducing finite barrier heights. In this case, the envelope function remains oscillatory inside the well and decays exponentially in the barrier regions, which leads to modified quantization conditions and ultimately enables tunnel coupling between neighboring wells.

In the finite-barrier case, the envelope function decays exponentially in the barrier regions. The corresponding decay constant is determined by the energy difference between the barrier height and the carrier energy projected onto the growth direction, and may be written as

$$\kappa^2 = \frac{2m_z^{(B)}}{\hbar^2}[V_0 - (E + E_\parallel)], \qquad E_\parallel = \frac{\hbar^2 k_x^2}{2m_\parallel} + \frac{\hbar^2 k_y^2}{2m_\parallel} \tag{18}$$

Here, $m_z^{(B)}$ is the effective mass in the barrier region along the growth direction, and κ determines the exponential decay of the envelope function outside the well. This quantity plays a key role in describing barrier penetration and the tunneling-induced coupling between neighboring wells in a superlattice. The finite-barrier description establishes the first part of the structure–property chain. The well width determines the confinement energy of the carrier states, while the barrier thickness controls the degree of envelope-function penetration into neighboring layers and, consequently, the tunneling probability between adjacent wells. A thinner barrier enhances interwell coupling and transforms discrete confined levels into dispersive minibands, whereas a thicker barrier suppresses coupling and drives the system toward the isolated quantum-well limit. The importance of barrier-controlled tunneling is also supported by theoretical studies of electron transport in two-barrier multilayer semiconductor structures, where layer thickness and barrier parameters determine carrier transmission [13]. Recent band-structure simulations of InAs/GaSb type-II superlattices further confirm that miniband dispersion and transition energies are strongly governed by layer thickness and the selected band model [14]. This thickness-dependent mechanism is consistent with the experimental analysis of InAs/InAsSb type-II superlattices by Webster et al., in which the miniband structure was calculated using a Kronig–Penney model and correlated with the measured absorption coefficient.

At each heterointerface, the envelope function must satisfy the standard BenDaniel–Duke boundary conditions, which ensure continuity of both the wave function and the probability current across the interface:

$$\psi_A = \psi_B, \qquad \frac{1}{m_A}\frac{d\psi}{dz}\Big|_A = \frac{1}{m_B}\frac{d\psi}{dz}\Big|_B \tag{19}$$

These interface conditions are used throughout the present superlattice analysis and provide the basis for deriving the miniband dispersion relation in the periodic structure. To describe a periodic superlattice, the interface boundary conditions in Eq. (19) must be supplemented by Bloch's theorem. For a superlattice period $d = a + b$, the envelope function satisfies

$$\phi_q(z + d) = e^{iqd}\phi_q(z), \qquad d = a + b, \qquad -\frac{\pi}{d} \le q \le \frac{\pi}{d} \tag{20a}$$

Let E_z denote the carrier energy associated with motion along the growth direction after subtraction of the in-plane kinetic energy: $E_z = E - \frac{\hbar^2 k_\parallel^2}{2m_\parallel}$. For the bound-miniband regime $0 < E_z < V_0$, the wave number in the well and the decay constant in the barrier are $k = \frac{\sqrt{2m_A E_z}}{\hbar}$, $\kappa = \frac{\sqrt{2m_B(V_0 - E_z)}}{\hbar}$. Using the state vector $Y(z) = \begin{pmatrix} \phi_q(z) \\ m^{-1}(z)\frac{d\phi_q(z)}{dz} \end{pmatrix}$, the propagation through one superlattice period can be written as $Y(z + d) = M(E_z)Y(z)$, where $\boldsymbol{M}(E_z)$ is the transfer matrix of one well–barrier period. Combining this relation with Bloch's theorem gives

$$\cos(qd) = \frac{1}{2}\mathrm{Tr}M(E_z) \tag{20b}$$

For a rectangular well of width a, a barrier of width b, and different effective masses in the two layers, evaluation of the transfer-matrix trace yields the following dispersion relation for $0 < E_z < V_0$:

$$\cos(qd) = \cos(ka)\cosh(\kappa b) + \frac{1}{2}\left(\frac{m_A\kappa}{m_B k} - \frac{m_B k}{m_A\kappa}\right)\sin(ka)\sinh(\kappa b) \tag{20c}$$

Equation (20c) is solved separately for electrons and heavy holes by using the corresponding conduction- and valence-band offsets and growth-direction effective masses. This procedure yields the electron and heavy-hole miniband dispersions $E_{e,i}(q)$ and $E_{hh,j}(q)$, respectively. Equation (20c) is the miniband dispersion relation of the periodic superlattice. For a specified Bloch wave vector q, its solutions determine the allowed carrier energies $E_n(q)$. The allowed minibands correspond to the energy intervals for which the right-hand side of Eq. (20c), denoted by $F(E_z)$, satisfies $|F(E_z)| \le 1$ whereas the intervals with

$|F(E_z)| > 1$ correspond to forbidden minigaps. Thus, interwell tunneling transforms each discrete confined level of an isolated quantum well into a finite-width miniband $E_n(q)$.

$$E_{ij}^{\mathrm{tr}}(q) = E_g^{\mathrm{II}} + E_{e,i}(q) + E_{hh,j}(q) \tag{20d}$$

As the barrier thickness increases, the envelope-function overlap between neighboring wells decreases and the miniband width becomes progressively smaller. In the weak-coupling limit, the allowed minibands collapse toward the discrete energy levels of the corresponding isolated finite quantum well given by Eqs. (8) and (9).

The tunneling-induced dispersion described by Eq. (20c) represents the optical-response extension of the superlattice concept introduced by Esaki and Tsu [15]. Because the allowed carrier energies depend on the Bloch wave vector q, the corresponding interband transition energies are distributed over finite energy intervals rather than concentrated at discrete quantum-well thresholds. This q - dependent dispersion provides the physical basis for the smoothing and broadening of the near-edge absorption spectrum derived below. The same mechanism is consistent with the experimental analysis of InAs/InAsSb type-II superlattices by Webster et al., who correlated the measured absorption coefficient with the calculated miniband structure and electron–hole wave-function overlap [18].

5. Formalism of Interband Optical Absorption.

Within the framework of quantum mechanics, the absorption coefficient associated with vertical interband optical transitions in semiconductors can, in general, be expressed in terms of the optical transition probability and the distribution of states. Within the single-particle picture, the absorption coefficient associated with vertical interband optical transitions can be expressed in terms of the transition probability and the occupation difference between the initial and final states as:

$$\alpha(\omega) = \frac{2\hbar\omega}{nc\varepsilon_0 F_0^2 V}\sum_k \sum_{i>j} \omega_{ji}(k)\left[f_0(E_{jk}) - f_0(E_{ik})\right] \tag{21}$$

Here, n is the refractive index of the medium, c is the speed of light, ε_0 is the vacuum permittivity, F_0 is the amplitude of the electromagnetic field, V is the normalization volume, and $f_0(E)$ is the Fermi–Dirac distribution function. The quantity $\omega_{ji}(k)$ denotes the probability of an optical transition from state $\boldsymbol{j}$ to state $\boldsymbol{i}$. According to Fermi's golden rule, the probability of an optical transition from state j to state i with wave vector k is given by

$$\omega_{ji}(k) = \frac{2\pi}{\hbar}\left(\frac{eF_0}{2m_0\omega}\right)^2 |P_{ij}(k)|^2 \delta(E_{ik} - E_{jk} - \hbar\omega) \tag{22}$$

Here, e is the elementary charge, m_0 is the free-electron mass, and $P_{ij}(k)$ is the matrix element of the momentum operator between the corresponding initial and final states. The delta function ensures conservation of energy during the optical transition.

The quantity $P_{ij}(k)$ entering Eq. (22) is the matrix element of the momentum operator between the corresponding initial and final states and is defined as

$$P_{ij}(k) = \int_V \psi_{ik}^*(r)\ (e \cdot \hat{p})\, \psi_{jk}(r)\, dV \tag{23}$$

Here, $\psi_{jk}(r)$ and $\psi_{ik}(r)$ are the wave functions of the initial and final states, respectively, $\hat{\boldsymbol{p}} = -\boldsymbol{i}\hbar\boldsymbol{\nabla}$ is the momentum operator, and $\boldsymbol{e}$ is the light-polarization unit vector. This matrix element determines the optical selection rules and the strength of the interband transition. For allowed direct interband transitions near the absorption edge, Eqs. (21)–(23) can be reduced to a simplified expression in which the spectral dependence is governed primarily by the momentum matrix element and the optical density of states:

$$\alpha(\omega) \simeq \frac{C}{\omega}\sum_{i,j} \left|P_{c_i v_j}\right|^2 \rho_{c_i v_j}(\omega) \tag{24}$$

Here, c and v denote the conduction and valence subbands, respectively, while C is a slowly varying prefactor that depends on the bulk optical parameters of the semiconductor. Equation (24) shows that the absorption spectrum near the edge is determined jointly by the transition strength and the available density of optically allowed states. The optical density of states for transitions between the valence subband $\boldsymbol{v_j}$ and the conduction subband c_i is defined by the number of states satisfying the energy-conservation condition and can be written as

$$\rho_{c_i v_j}(\omega) = \sum_k \delta\left(E_{c_i}(k) - E_{v_j}(k) - \hbar\omega\right) \tag{25}$$

This quantity determines the number of optically allowed transitions contributing to absorption at a given photon energy $\hbar\omega$. The delta function selects only those states for which the interband transition energy matches the photon energy. Equivalently, the optical density of states may be represented as the derivative of the number of optically allowed transitions with respect to the photon energy:

$$\rho_{c_i v_j}(\omega) = \frac{d}{d(\hbar\omega)} \sum_k \Theta\left[\hbar\omega - \left(E_{c_i}(k) - E_{v_j}(k)\right)\right] \tag{26}$$

This representation is especially convenient for analyzing threshold behavior, since it makes explicit that the optical density of states is determined by the accumulation of interband transitions as the photon energy increases..

This formalism serves as the basis for analyzing the characteristics of the interband optical absorption spectrum in quantum wells and superlattices in the following sections. The absorption coefficient derived in this section corresponds to an experimentally measurable optical quantity. Webster et al. determined the absorption coefficients of InAs/InAsSb type-II superlattices from room-temperature spectroscopic ellipsometry measurements, making their results directly relevant to the present theoretical framework. In this formulation, the absorption coefficient is governed by the optical transition probability, the density of optically allowed states, and the electron–hole envelope-function overlap. This connection indicates that the present absorption formalism provides a physically grounded basis for interpreting experimentally measured absorption spectra of type-II superlattice heterostructures.

5.1. Absorption in Isolated Quantum Wells

In isolated quantum wells, interband optical absorption is governed by vertical optical transitions from the valence band to the conduction band. The intensity of this process depends on the structure of the wave functions, their overlap, and the optical density of states. In an isolated quantum well, the initial valence-subband state participating in an interband optical transition can be written in the factorized form:

$$\psi_{v j k_\parallel}(r) = \frac{1}{\sqrt{S}} e^{i k_\parallel \cdot \rho} \phi_{v j}(z) u_v(r) \tag{27}$$

Here, $\rho = (x, y)$ is the in-plane coordinate, $k_\parallel$ is the corresponding in-plane wave vector, $\phi_{v_j}(z)$ is the envelope function of the j-th valence subband, and $u_v(r)$ is the periodic Bloch function of the valence band. The corresponding final state in the conduction subband is written in an analogous form as

$$\psi_{c i k_\parallel}(r) = \frac{1}{\sqrt{S}} e^{i k_\parallel \cdot \rho} \phi_{c i}(z) u_c(r) \tag{28}$$

Here, $\phi_{c_i}(z)$ is the envelope function of the i-th conduction subband, and $u_c(r)$ is the periodic Bloch function of the conduction band. Together, Eqs. (27) and (28) define the basis states for calculating the interband transition matrix elements in a quantum well. The energy dispersion of the j-th valence subband in an isolated quantum well can be written as

$$E_{v j}(k_\parallel) = E_v - E_{v j} - \frac{\hbar^2 k_\parallel^2}{2 m_p} \tag{29}$$

Here, E_{v_j} is the confinement energy of the $\boldsymbol{j}$-th valence subband measured downward from the valence-band edge, and the second term describes the in-plane kinetic energy of the hole. Similarly, the energy dispersion of the i-th conduction subband is given by

$$E_{c i}(k_\parallel) = E_c + E_{c i} + \frac{\hbar^2 k_\parallel^2}{2 m_n} \tag{30}$$

Here, E_{c_i} is the confinement energy of the i-th conduction subband measured upward from the conduction-band edge, and the last term represents the in-plane kinetic energy of the electron. Substituting the wave functions given by Eqs. (27) and (28) into the momentum-operator matrix element, one obtains the factorized expression

$$P_{c i v j}(k_\parallel) = P_{cv} S_{c_i v_j} \tag{31}$$

Here, P_{cv} is the bulk interband momentum matrix element, whereas $S_{c_i v_j}$ is the overlap integral of the envelope functions. This factorization shows that the probability of an interband transition in a quantum well is determined jointly by the bulk band-structure properties and the confinement-induced overlap of the subband wave functions. The quantity $\boldsymbol{P_{cv}}$ entering Eq. (31) is the bulk interband momentum matrix element and is defined by

$$P_{cv} = \frac{1}{\Omega} \int_\Omega u_c^*(r)\ (e \cdot \hat{p})\, u_v(r)\, dV \tag{32}$$

Here, $u_c(r)$ and $u_v(r)$ are the periodic Bloch functions of the conduction and valence bands, respectively, and Ω is the unit-cell volume. This quantity determines the intrinsic transition strength in the corresponding bulk semiconductor. The quantity $S_{c_i v_j}$ in Eq. (31) is the overlap integral of the envelope functions associated with the corresponding conduction and valence subbands and is given by

$$S_{c_i v_j} = \int_L \phi^*_{c_i}(z)\ \phi_{v_j}(z)\, dz \tag{33}$$

This overlap integral determines the additional optical selection rules introduced by quantum confinement. Its value depends on the spatial symmetry and localization of the envelope states along the growth direction. In the idealized approximation of an infinitely deep symmetric quantum well, the envelope functions form an orthonormal set, and the overlap integral reduces to

$$S_{c_i v_j} = \delta_{ij} \tag{34}$$

Equation (34) shows that, in the infinite-well limit, interband optical transitions are strongest between subbands with the same ordinal number. In finite wells, however, barrier penetration relaxes this strict selection rule and allows weaker transitions between states of different index but compatible parity. The sensitivity of interband absorption to confinement potential, band offsets, and well asymmetry has also been reported for wurtzite MgZnO/ZnO asymmetric quantum wells, where structural parameters strongly modify the transition energies and absorption strength [16]. Using the factorized form of the interband matrix element, the absorption coefficient near the intrinsic absorption edge of an isolated quantum well can be written as

$$\alpha_{cv}(\omega) = \frac{2\pi e^2\,|P_{cv}|^2}{nc\varepsilon_0 m_0^2\,\omega\,V} \sum_{i,j} \left|S_{c_i v_j}\right|^2\ \rho_{c_i v_j}(\omega) \tag{35}$$

Here, $\rho_{c_i v_j}(\omega)$ is the optical density of states for transitions between the $\boldsymbol{j}$-th valence subband and the $\boldsymbol{i}$-th conduction subband. Equation (35) shows that the absorption strength is determined by the combined effect of the bulk interband coupling, the envelope-function overlap, and the density of optically allowed final states. This step-like interband absorption behavior is consistent with the established theory of linear optical properties in semiconductor quantum wells, where subband quantization, optical matrix elements, and envelope-function overlap play central roles in determining the absorption spectrum [17]. For an isolated quantum well, substitution of the parabolic subband dispersions given by Eqs. (29) and (30) into the definition of the optical joint density of states yields the following expression per unit area:

$$\rho_{ij}^{2D}(\hbar\omega) = \frac{g_s}{A}\sum_{k_\parallel} \delta\left[E_{c_i}(k_\parallel) - E_{v_j}(k_\parallel) - \hbar\omega\right] \tag{36a}$$

The transition energy associated with the in-plane wave vector $k_\parallel$ can be written as

$$E_{c_i}(k_\parallel) - E_{v_j}(k_\parallel) = E_{cv}^{(ij)} + \frac{\hbar^2 k_\parallel^2}{2\mu_{ij}}$$

where

$$E_{cv}^{(ij)} = E_g + E_{c_i}^{(z)} + E_{h_j}^{(z)}$$

is the threshold energy for the transition between the $\boldsymbol{j}$-th valence subband and the $\boldsymbol{i}$-th conduction subband. Replacing the summation over the in-plane wave vectors by the two-dimensional integral

$$\frac{1}{A}\sum_{k_\parallel} \rightarrow \frac{1}{(2\pi)^2}\int d^2\, k_\parallel$$

and evaluating the delta-function integral gives.

$$\rho_{ij}^{2D}(\hbar\omega) = \frac{g_s\mu_{ij}}{2\pi\hbar^2}\,\Theta\left(\hbar\omega - E_{cv}^{(ij)}\right) = \frac{\mu_{ij}}{\pi\hbar^2}\,\Theta\left(\hbar\omega - E_{cv}^{(ij)}\right), \qquad g_s = 2 \tag{36b}$$

Equation (36b) is the two-dimensional optical joint density of states per unit area and per unit photon energy, with the spin degeneracy $g_s = 2$ included explicitly. The Heaviside step function $\Theta\left(\hbar\omega - E_{cv}^{(ij)}\right)$ is zero below the transition threshold and constant above it. Consequently, each optically allowed pair of electron and hole subbands produces a discrete step in the optical joint density of states. This constant two-dimensional density of states is the physical origin of the staircase-like near-edge absorption spectrum of an ideal quantum well. The in-plane reduced mass μ_{ij} entering Eq. (36b) is defined by

$$\frac{1}{\mu_{ij}} = \frac{1}{m_{e,i}^{\parallel}} + \frac{1}{m_{h,j}^{\parallel}} \tag{37}$$

Here, $m_{e,i}^{\parallel}$ and $m_{h,j}^{\parallel}$ are the in-plane effective masses of the electron and hole subbands, respectively. This quantity determines the prefactor of the two-dimensional optical density of states and therefore governs the magnitude of each step in the absorption spectrum near the threshold. Substituting the two-dimensional optical joint density of states given by Eq. (36b) into Eq. (35), the absorption coefficient near the intrinsic absorption edge takes the step-like form

$$\alpha_{cv}(\omega) = A_{cv} \sum_{ij} \left| S_{c_i v_j} \right|^2 \Theta\left(\hbar\omega - E_{cv}^{(ij)}\right) \tag{38}$$

Here, $E_{cv}^{(ij)}$ is the threshold photon energy for an interband transition between the $\boldsymbol{j}$-th valence subband and the $\boldsymbol{i}$-th conduction subband. Equation (38) explicitly shows that each allowed interband transition contributes a separate step to the absorption spectrum.

Figure 4 schematically illustrates the step-like behavior of the interband optical absorption coefficient in an isolated semiconductor quantum well. Each step begins at the threshold energy of the corresponding allowed transition between quantized valence and conduction subbands. This spectral form originates from the two-dimensional optical density of states and reflects the confinement-induced discretization of the carrier energy spectrum. As a consequence, the absorption edge is shifted toward higher photon energies relative to the bulk semiconductor and acquires a staircase-like dependence on photon energy.

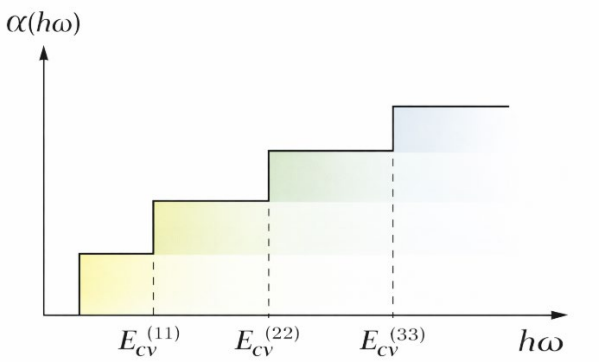

Figure 4. Schematic spectrum of the interband optical absorption coefficient in an isolated semiconductor quantum well. The absorption exhibits a step-like dependence on photon energy, where each step begins at the threshold energy of the corresponding interband transition between quantized valence and conduction subbands.

Because Eq. (36b) defines the joint density of states per unit area, conversion to the volume-normalized absorption coefficient is incorporated through the factor $1/a$ contained in the optical prefactor in Eq. (39). The prefactor A_{cv} in Eq. (39) is determined by the bulk optical parameters of the semiconductor and can be written as

$$A_{cv} = \frac{m_{\mathrm{op}}\, e^2\, |P_{cv}|^2}{nc\varepsilon_0 m_0^2\, \hbar E_g\, a} \tag{39}$$

Here, $\boldsymbol{a}$ is the quantum-well width, and the prefactor A_{cv} determines the magnitude of each absorption step. Equation (39) shows that the spectral weight of the interband absorption depends on both the bulk interband coupling strength and the geometric confinement of the quantum well. Here, m_{op} denotes the in-plane optical reduced mass and is identified with μ_{ij} defined in Eq. (37).

According to Eq. (38), the interband absorption spectrum of an isolated quantum well near the intrinsic absorption edge exhibits the following characteristic features (Fig. 4).

A. The absorption edge is shifted toward higher photon energies relative to the bulk semiconductor because the allowed interband transitions begin at the quantized subband thresholds rather than at the bulk band gap.

B. The absorption coefficient acquires a step-like spectral form in the threshold region, with each step corresponding to transitions between specific valence and conduction subbands.

C. Within the present single-particle approximation, the near-edge spectral shape is governed primarily by the subband structure and the two-dimensional optical density of states, while finer effects such as excitonic contributions and temperature-induced broadening are not included explicitly.

D. In symmetric quantum wells, additional optical selection rules are determined by the spatial symmetry of the envelope functions, so that transitions between subbands of the same parity are favored.

Thus, in isolated quantum wells, the spectrum of interband optical absorption is shifted relative to that of the bulk semiconductor due to the quantum-size effect and acquires a step-like form.

5.2. Absorption in Periodic Superlattices

In periodic superlattices composed of coupled quantum wells, interband optical absorption differs from that in isolated quantum wells because the discrete confined states broaden into minibands as a result of tunneling between adjacent wells. Consequently, the optical response acquires a characteristic dependence on miniband dispersion along the growth direction. In a periodic superlattice, the initial valence-miniband state participating in an interband optical transition can be represented by a Bloch-type envelope function of the form

$$\psi_{vjk}(r) = \frac{1}{\sqrt{V}} e^{ik_{\parallel}\cdot\rho} \phi_{vjq}(z) u_v(r) \tag{40}$$

Here, $\rho = (\boldsymbol{x}, \boldsymbol{y})$ is the in-plane coordinate**,** $k_{\parallel}$ is the corresponding in-plane wave vector, $\boldsymbol{q}$ is the Bloch wave vector along the superlattice direction, $\boldsymbol{\phi_{v_jq}(z)}$ is the envelope function of the $\boldsymbol{j}$-th valence miniband, and $\boldsymbol{u_v(r)}$ is the periodic Bloch function of the valence band. The corresponding final state in the conduction miniband is written in the analogous form

$$\psi_{cik}(r) = \frac{1}{\sqrt{V}} e^{ik_{\parallel}\cdot\rho} \phi_{ciq}(z) u_c(r) \tag{41}$$

Here, $\boldsymbol{\phi_{c_iq}(z)}$ is the envelope function of the $\boldsymbol{i}$-th conduction miniband, and $\boldsymbol{u_c(r)}$ is the periodic Bloch function of the conduction band. Together, Eqs. (40) and (41) define the miniband states entering the interband absorption process in a superlattice. The energy dispersion of the $\boldsymbol{j}$-th valence miniband in a periodic superlattice can be written as

$$E_{vj}(k) = E_v - E_{vj}(q) - \frac{\hbar^2 k_{\parallel}^2}{2m_p} \tag{42}$$

Here, $\boldsymbol{E_{v_j}(q)}$ describes the miniband dispersion along the growth direction, while the last term represents the in-plane kinetic energy. This form shows that the valence-band states remain free in the plane of the layers but become dispersive along the superlattice axis because of interwell coupling. Similarly, the energy dispersion of the $\boldsymbol{i}$-th conduction miniband is given by

$$E_{ci}(k) = E_c + E_{ci}(q) + \frac{\hbar^2 k_{\parallel}^2}{2m_n} \tag{43}$$

Here, $\boldsymbol{E_{c_i}(q)}$ is the miniband dispersion of the $\boldsymbol{i}$-th conduction state along the superlattice direction, while the last term represents the in-plane kinetic energy of the electron. In contrast to the isolated quantum-well case, the dependence on $\boldsymbol{q}$ reflects the broadening of discrete subband levels into minibands due to tunneling between adjacent wells.

For a superlattice composed of weakly coupled quantum wells, the absorption coefficient can be written in a form analogous to that for an isolated quantum well, but with the overlap integrals and prefactor modified by the miniband structure:

$$\alpha_{cv}^{\mathrm{SL}}(\hbar\omega) = A_{cv}^{\mathrm{SL}} \sum_{i,j} \left| S_{c_i v_j}^{\mathrm{SL}} \right|^2 \Theta\left(\hbar\omega - E_{cv}^{(ij)}\right) \tag{44}$$

Here, A_{cv}^{SL} is the optical prefactor for the superlattice, while $S_{c_i v_j}^{\mathrm{SL}}$ is the effective overlap integral for transitions between the corresponding valence and conduction minibands. In comparison with the isolated-well case, these quantities are modified by interwell tunneling and miniband dispersion.

Equation (44) represents the simplified weak-coupling limit, where miniband dispersion is neglected. In a real periodic superlattice, however, the confined quantum-well levels broaden into minibands due to interwell tunneling. Therefore, the transition energy depends on the Bloch wave vector q along the growth direction:

$$E_{ij}^{SL}(q) = E_g + E_{ci}(q) + E_{vj}(q) \tag{45}$$

Accordingly, the absorption coefficient should be written as an expression integrated over the Bloch wave vector q:

$$\alpha_{SL}(\hbar\omega) = A_{cv}^{SL} \sum_{i,j} \int_{-\pi/d}^{\pi/d} \left| S_{ij}^{SL}(q) \right|^2 \rho_{ij}^{2D} \Theta_{\Gamma}\left[\hbar\omega - E_{ij}^{SL}(q)\right] \frac{dq}{2\pi/d} \tag{46}$$

Here, $d = a + b$ is the superlattice period, $S_{ij}^{SL}(q)$ is the electron–hole envelope-function overlap, and ρ_{ij}^{2D} is the in-plane optical density of states. Here, $\Theta_\Gamma(x)$ denotes the Lorentzian-broadened Heaviside threshold function. It is obtained by integrating the normalized Lorentzian line-shape function $\boldsymbol{L_\Gamma(x)}$, where $\boldsymbol{\Gamma}$ is the full width at half maximum.

$$\Theta_\Gamma(x) = \int_{-\infty}^{x} L_\Gamma(u)\, du = \frac{1}{2} + \frac{1}{\pi}\arctan\left(\frac{2x}{\Gamma}\right) \tag{47}$$

For each fixed Bloch wave vector $\boldsymbol{q}$, integration over the continuous in-plane carrier states produces a two-dimensional step-like absorption contribution. To account for spectral broadening, this Heaviside threshold is convoluted with the normalized Lorentzian line-shape function. The resulting Lorentzian-broadened threshold function is denoted by $\boldsymbol{\Theta_\Gamma(x)}$, where $\boldsymbol{\Gamma}$ is the full width at half maximum.

This treatment does not introduce an additional optical mechanism; it provides the broadened form of the two-dimensional threshold already obtained for the isolated quantum well. Integration over the $\boldsymbol{q}$ -dependent transition energies and envelope-function overlaps leads to the gradual absorption onset and high-energy plateau shown in Fig. 7.

As a result, the sharp step-like absorption edge of an isolated quantum well becomes smoother and broader in a superlattice. Experimental studies of III–V quantum wells and superlattices have likewise shown that interwell coupling and the resulting miniband structure substantially modify the near-edge absorption and electroabsorption spectra [19].

For weakly coupled superlattices, the optical prefactor and the effective overlap integral may be related to the corresponding isolated-well quantities through the superlattice period as

$$A_{cv}^{\mathrm{SL}} = \frac{a}{d}\, A_{cv}, \qquad S_{c_i v_j}^{\mathrm{SL}}(\mathrm{q}) \approx \frac{1}{d}\int_{-d/2}^{d/2} \phi_{c_i q}^{*}(z)\; \phi_{v_j q}(z)\, dz \tag{48}$$

Equations (46)–(48), together with the electron and heavy-hole miniband dispersions obtained from Eq. (20c), form the basis of the numerical calculation of the interband absorption response. The numerical procedure and the structural and material parameters used in the calculations are described below. The close connection between infrared absorption and miniband dispersion has also been demonstrated experimentally, confirming that optical spectroscopy can be used as a sensitive probe of the electronic miniband structure in semiconductor superlattices [20].

6. Numerical Method and Material Parameters

6.1. Numerical Solution of the Miniband Dispersion Equation

The miniband dispersion relation given by Eq. (20c) was solved numerically and separately for electrons and heavy holes. For electrons, the conduction-band offset and the corresponding electron effective masses in the well and barrier layers were used, whereas the valence-band offset and the growth-direction heavy-hole effective masses were used for the hole calculation. The numerical analysis was performed over one half of the first Brillouin zone, $0 \le q \le \pi/d$, because the miniband energies satisfy the symmetry relation $E_n(-q) = E_n(q)$.

$$q_r = \frac{r\pi}{200d}, \qquad r = 0,1,\ldots,200 \tag{49}$$

Thus, the normalized Bloch wave vector $\boldsymbol{qd/\pi}$ was sampled using 201 uniformly spaced points with an increment of 0.005. For each $\boldsymbol{q_r}$, Eq. (20c) was rewritten as a scalar root equation

$$G_s(E; q_r) = F_s(E) - \cos(q_r d) = 0, \qquad s = e,\mathrm{hh} \tag{50}$$

where $\boldsymbol{F_e(E)}$ and $\boldsymbol{F_{hh}(E)}$ are the right-hand sides of the Kronig–Penney dispersion relation for electrons and heavy holes, respectively. The bound-state search intervals were $\boldsymbol{0 < E_e < \Delta E_c}$ for electrons and $\boldsymbol{0 < E_{hh} < \Delta E_v}$ for heavy holes. All sign-changing intervals were first identified by an energy scan, and each root was subsequently refined using a bracketed Brent algorithm. The roots were sorted by increasing energy and continuously tracked as a function of q to obtain $\boldsymbol{E_{e,i}(q)}$ and $\boldsymbol{E_{hh,j}(q)}$. The absolute energy tolerance of the root solver was set to $\boldsymbol{10^{-10}eV}$.

6.2. Wave-Function Normalization and Electron–Hole Overlap

For every calculated miniband energy, the corresponding envelope function was reconstructed from the eigenvector of the one-period transfer matrix satisfying

$$\left[M_s\left(E_{s,n}(q)\right) - e^{iqdI}\right] Y_s(0) = 0, \qquad s = e,\text{hh} \tag{51}$$

The state vector was propagated through the well and barrier layers using the corresponding layer transfer matrices. The electron and heavy-hole envelope functions were normalized over one superlattice period according to

$$\int_0^d \left|\phi_{s,n,q}(z)\right|^2 \, dz = 1, \qquad s = e,\text{hh} \tag{52}$$

The envelope-function overlap for a vertical transition between the $\boldsymbol{i}$-th electron miniband and the j-th heavy-hole miniband was then evaluated as

$$S_{ij}(q) = \int_0^d \phi^*_{e,i,q}(z)\phi_{\text{hh},j,q}(z) \, dz \tag{53}$$

The optical transition probability was weighted by the dimensionless quantity $\left|\boldsymbol{S_{ij}(q)}\right|^2$. The ground-state analysis was based primarily on the $\boldsymbol{e_1 - hh_1}$ transition. The spatial integrations were performed using a uniform grid of 4001 points over one superlattice period. The calculation was repeated using 8001 points to verify numerical convergence.

6.3. Numerical Evaluation of the Absorption Coefficient

The $\boldsymbol{q}$-dependent ground-state transition energy was calculated as

$$E_{11}^{\text{tr}}(q) = E_g^{\text{II}} + E_{e,1}(q) + E_{\text{hh},1}(q) \tag{54}$$

where $\boldsymbol{E_g^{\text{II}}}$ is the type-II band-edge separation between the electron-confining and hole-confining layers. The ground-state absorption spectrum was evaluated by numerically integrating Eq. (46) over the first Brillouin zone. The normalized Lorentzian function defined in Eq. (55) was used as the broadening kernel for the two-dimensional threshold function $\boldsymbol{\Theta_\Gamma}$ introduced in Eq. (47).

$$L_\Gamma(x) = \frac{1}{\pi}\frac{\Gamma/2}{x^2 + (\Gamma/2)^2} \tag{55}$$

where $\boldsymbol{\Gamma}$ denotes the full width at half maximum (FWHM). A fixed value of $\boldsymbol{\Gamma = 4.0}$ meV, corresponding to an HWHM of 2.0 meV, was used in all absorption calculations. The absorption coefficient was evaluated on a uniform photon-energy grid from 80 to 130 meV with an energy step of 0.05 meV.

6.4. Structural and Material Parameters

The detailed $\boldsymbol{q}$-resolved numerical calculation was performed for the InAs/InAsSb type-II superlattice corresponding to sample B. This sample was selected because its room-temperature absorption spectrum and the assignments of the principal miniband transitions were reported in detail by Webster et al. The structural and optical quantities used for comparison are summarized in Table 1.

The refined structural parameters, including the unintentional incorporation of Sb into the nominal InAs layers, were taken from the subsequent detailed X-ray diffraction and band-edge analysis of Webster et al. [27].

Table 1. Structural and experimental parameters of sample B used for numerical modelling and validation

Quantity	**Webster et al. (2015)**	**Numerical input**	**Unit**
Sb mole fraction in InAsSb	0.284	0.263	—
Unintentional Sb fraction in InAs	not reported	0.008	—
InAs layer thickness	17.18	17.16	nm
InAsSb layer thickness	7.32	7.34	nm
Superlattice period (d)	24.50	24.50	nm
Temperature	295	295	K
Ground-state absorption onset	103	—	meV
Ground-state absorption coefficient	456	—	cm^{-1}
Ground-state overlap squared	0.081	—	—

The small differences between the originally reported structural values and the numerical inputs arise from the subsequently refined structural parameter set used in the band-structure calculation.

Table 2. Band-edge and effective-mass parameters used for sample B

Parameter	Symbol	Value	Unit	Source

Type-II band-edge separation	E_g^{II}	64.7588	meV	Ref. [27]/present calculation
Electron barrier height	ΔE_c	119.3113	meV	Ref. [27]/present calculation
Heavy-hole barrier height	ΔE_v	271.6350	meV	Ref. [27]/present calculation
Electron effective mass in $InAs_{\mathbf{0.992}}Sb_{\mathbf{0.008}}$ electron well	$m_{e,w}^*$	0.02562	m_0	Composition-interpolated value
Electron effective mass in $InAs_{\mathbf{0.737}}Sb_{\mathbf{0.263}}$ electron barrier	$m_{e,b}^*$	0.01593	m_0	Composition-interpolated value
Heavy-hole effective mass in $InAs_{\mathbf{0.737}}Sb_{\mathbf{0.263}}$ hole well	$m_{hh,w}^*$	0.31486	m_0	Composition-interpolated value
Heavy-hole effective mass in $InAs_{\mathbf{0.992}}Sb_{\mathbf{0.008}}$ hole barrier	$m_{hh,b}^*$	0.33274	m_0	Composition-interpolated value
Lorentzian broadening FWHM	Γ_{FWHM}	4.0	meV	present calculation

Note: The electron effective masses were evaluated using composition-dependent quadratic interpolation with the effective-mass bowing correction, whereas the heavy-hole effective masses were obtained by linear interpolation between the corresponding binary InAs and InSb values. The refined Sb mole fractions of 0.008 and 0.263 were used for the nominal InAs and InAsSb layers of sample B, respectively. Here, m_0 denotes the free-electron mass.

The effective masses listed in Table 2 correspond to carrier motion along the superlattice growth direction. Because of the type-II band alignment, electrons are predominantly confined in the $InAs_{0.992}Sb_{0.008}$ layers, whereas heavy holes are localized mainly in the $InAs_{0.737}Sb_{0.263}$ layers. The layer-dependent effective masses and band offsets were used consistently in the transfer-matrix calculation of the electron and heavy-hole miniband dispersions. A fixed Lorentzian broadening parameter of $\Gamma = 4.0\ meV$ was adopted in the numerical evaluation of the absorption coefficient.

Numerical convergence was examined by repeating the calculations with denser Bloch-wave-vector and spatial grids. The calculation was regarded as converged when the changes in the miniband-edge energies were below 10^{-4} meV and the change in the ground-state overlap squared was below 10^{-5}.

7. Numerical Results and Experimental Validation

The numerical procedure described in Section 6 was applied to the InAs/InAsSb type-II superlattice corresponding to sample B. The calculated electron and heavy-hole miniband dispersions, ground-state transition energy, electron–hole wave-function overlap, and absorption response are presented first. The model is then quantitatively evaluated using the room-temperature data reported by Webster et al. for ten InAs/InAsSb superlattices.

7.1. Electron and Heavy-Hole Miniband Dispersions

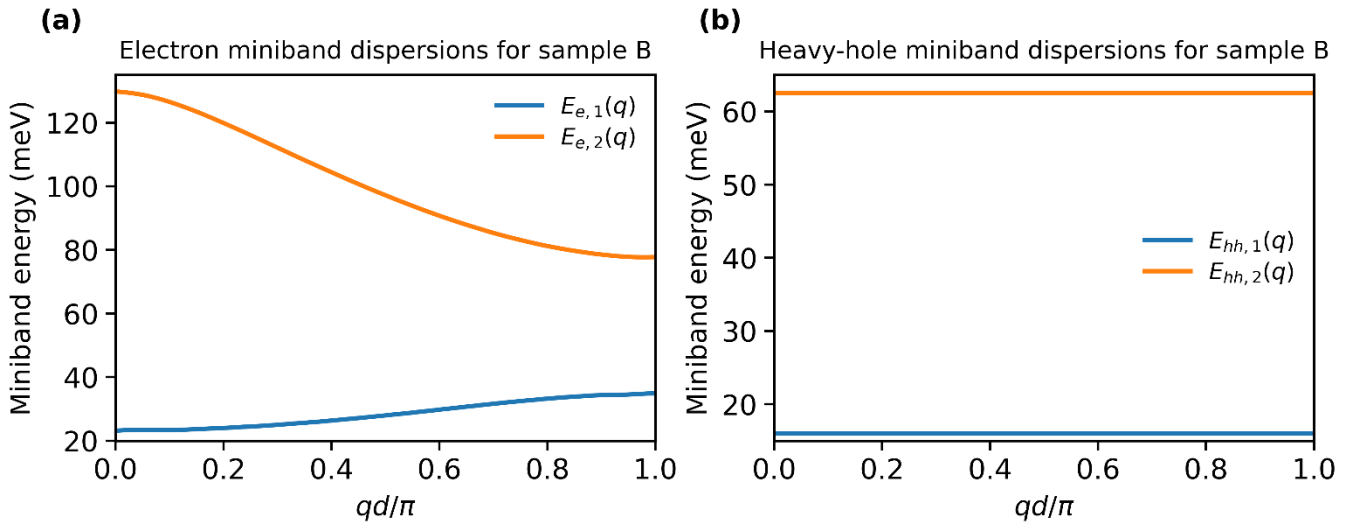

Figure 5. Calculated miniband dispersions of the InAs/InAsSb type-II superlattice corresponding to sample B at 295 K. (a) First and second electron minibands, $E_{e,1}(q)$ and $E_{e,2}(q)$. (b) First and second heavy-hole minibands, $E_{hh,1}(q)$ and $E_{hh,2}(q)$, over one half of the first Brillouin zone.

As shown in Fig. 5, the calculated miniband dispersions differ substantially for electrons and heavy holes. The first electron miniband increases from $21.7316\ meV$ at the Brillouin-zone centre to $33.2893\ meV$ at the zone boundary, corresponding to a miniband width of $11.5577\ meV$. The second electron miniband also exhibits a clear q -dependent dispersion. In contrast, the first heavy-hole miniband remains practically dispersionless at $15.6907\ meV$ within the numerical resolution of the calculation, while the second heavy-hole miniband shows only a weak variation with q. This difference reflects the much larger growth-direction effective mass of heavy holes and indicates that the ground-state optical-transition dispersion is governed predominantly by the electron miniband.

7.2. Ground-State Transition Energy and Wave-Function Overlap

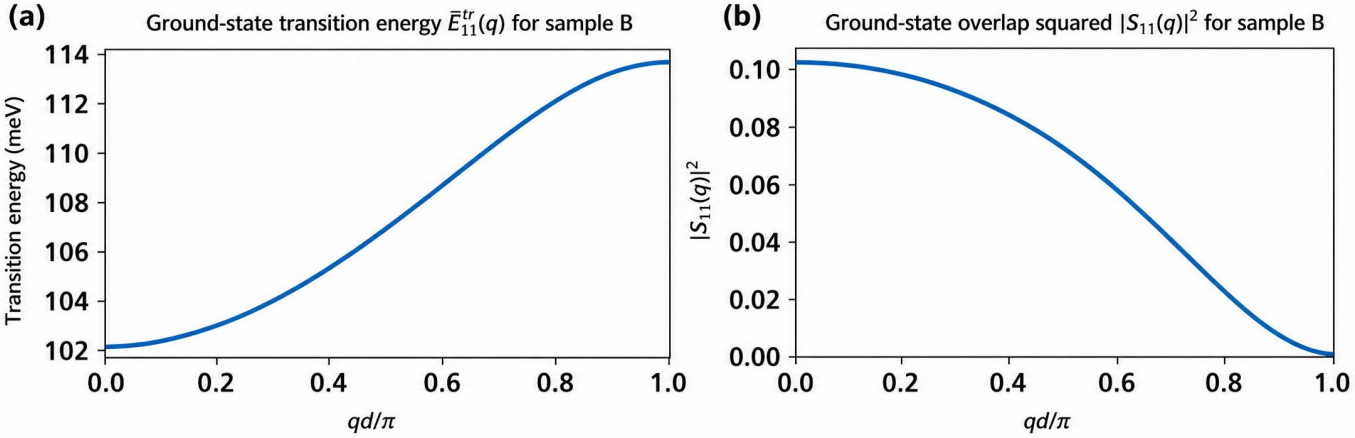

Figure 6. Calculated ground-state optical-transition characteristics of the InAs/InAsSb type-II superlattice corresponding to sample B at 295 K. (a) Ground-state transition-energy dispersion, $E_{11}^{\mathrm{tr}}(q)$. (b) Electron–heavy-hole envelope-function overlap squared, $|S_{11}(q)|^2$, plotted over one half of the first Brillouin zone as a function of the normalized Bloch wave vector qd/π.

Figure 6 shows the calculated q -dependent characteristics of the ground-state optical transition in sample B. As seen in Fig. 6(a), the transition energy $E_{11}^{\mathrm{tr}}(q)$ increases from $102.1811\ meV$ at the Brillouin-zone centre to $113.7388\ meV$ at the zone boundary, reflecting the finite dispersion of the electron miniband. In contrast, Fig. 6(b) shows that the electron–heavy-hole overlap squared decreases monotonically with increasing q, from a maximum value of 0.101788 at $q = 0$ to nearly zero near the zone boundary. The Brillouin-zone-averaged value is $\langle |S_{11}(q)|^2 \rangle = 0.061261$. These results indicate that the optical absorption strength is governed not only by the transition-energy distribution within the miniband, but also by the

strong q -dependence of the envelope-function overlap. Consequently, states located in different parts of the miniband contribute unequally to the absorption spectrum.

7.3. Calculated Ground-State Absorption Response

The room-temperature ground-state absorption response of sample B was calculated by numerically integrating the q - dependent absorption expression in Eq. (46), using the transition-energy dispersion $E_{11}^{\mathrm{tr}}(q)$ and the envelope-function overlap squared $|S_{11}(q)|^2$ presented in Fig. 6. For the calculated curve shown below, the two-dimensional absorption threshold was broadened using the normalized Lorentzian kernel with an FWHM of $\boldsymbol{\Gamma = 4.0\ meV}$, and the photon-energy interval from 80 to 130 meV was sampled with a step of 0.05 meV. The resulting absorption response is shown in Fig. 7.

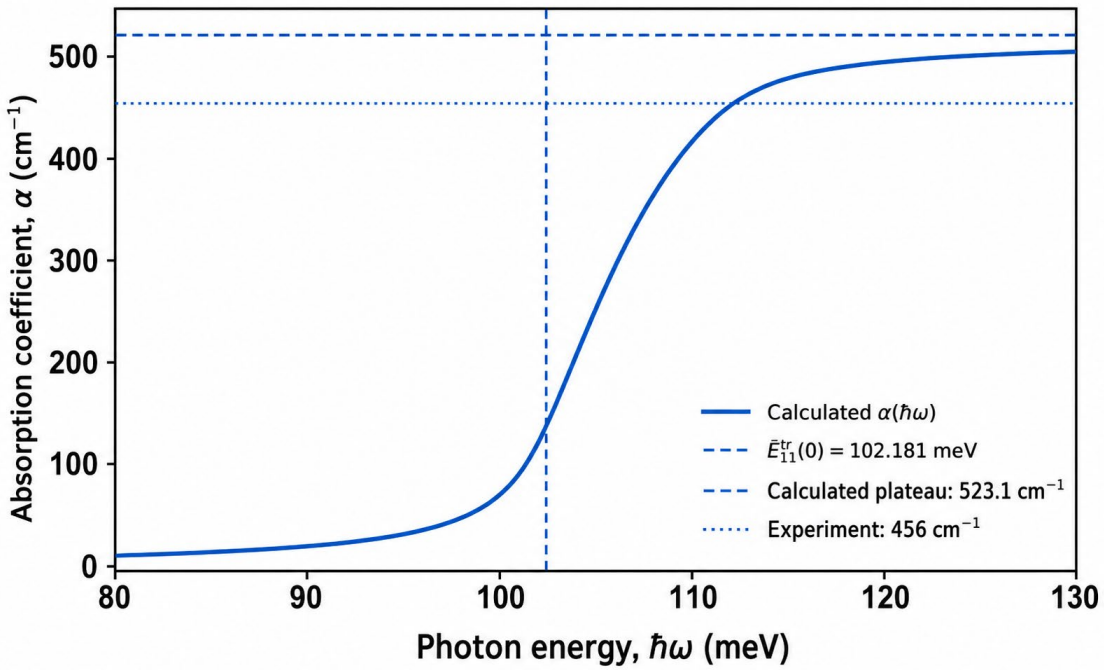

Figure 7. Calculated room-temperature ground-state absorption response $\boldsymbol{\alpha(\hbar\omega)}$ of the InAs/InAsSb type-II superlattice corresponding to sample B. The vertical dashed line indicates the calculated $e_1 - hh_1$ transition threshold, $E_{11}^{\mathrm{tr}}(0) = 102.181 meV$. The horizontal dashed and dotted lines indicate the calculated absorption plateau of $523.1\ \mathrm{cm}^{-1}$ and the experimentally reported ground-state absorption coefficient of $456\ \mathrm{cm}^{-1}$, respectively. A Lorentzian full width at half maximum of $\boldsymbol{\Gamma = 4.0}\ meV$, corresponding to an HWHM of 2.0 meV, was used.

As shown in Fig. 7, the calculated absorption coefficient begins to increase in the vicinity of the ground-state transition energy $E_{11}^{\mathrm{tr}}(0) = 102.1811 meV$ and gradually approaches a plateau value of $523.1\ \mathrm{cm}^{-1}$. The smooth onset results from the combined effects of miniband dispersion, the q - dependent electron–heavy-hole overlap, and the Lorentzian spectral broadening. The calculated transition threshold differs from the experimentally measured absorption onset of $103\ meV$ by only $0.819\ meV$. The calculated plateau exceeds the reported experimental ground-state absorption coefficient of $456\ \mathrm{cm}^{-1}$ by $67.1\ \mathrm{cm}^{-1}$, corresponding to a relative difference of 14.71%.

Webster et al. reported that the ground-state absorption of sample B rises sharply to $456\ \mathrm{cm}^{-1}$ at the $e_1 - hh_1$ transition and estimated an uncertainty of approximately $\pm 20\%$ for the measured absorption coefficients. Therefore, the calculated value lies within the reported experimental uncertainty. The remaining difference may originate from the simplified single-particle effective-mass model, the use of phenomenological broadening, and the neglect of interface roughness, alloy disorder, multiband coupling, and excitonic effects.

7.4. Quantitative Validation Using Published InAs/InAsSb Data

To evaluate the overlap-controlled absorption relationship across structurally different superlattices, the room-temperature data reported by Webster et al. for ten InAs/InAsSb type-II superlattices were reanalysed. The measured ground-state absorption coefficients and the corresponding ground-state

electron–heavy-hole wave-function overlap squares were taken from Table I of Ref. [18]. The overlap values were calculated by Webster et al. using a Kronig–Penney model, whereas the absorption coefficients were determined experimentally by spectroscopic ellipsometry at 295 K. Therefore, the present analysis represents an independent statistical reanalysis of the published data rather than a new calculation of the A–J overlap values.

Because the absorption strength is expected to vanish as the electron–hole overlap approaches zero within the present model, the data were fitted using the following zero-intercept linear relation:

$$\alpha_{GS} = C|S_{11}|^2 \tag{56}$$

Here, C is the fitted proportionality coefficient, α_{GS} is the measured ground-state absorption coefficient, and $|\boldsymbol{S_{11}}|^2$ is the calculated ground-state wave-function overlap squared.

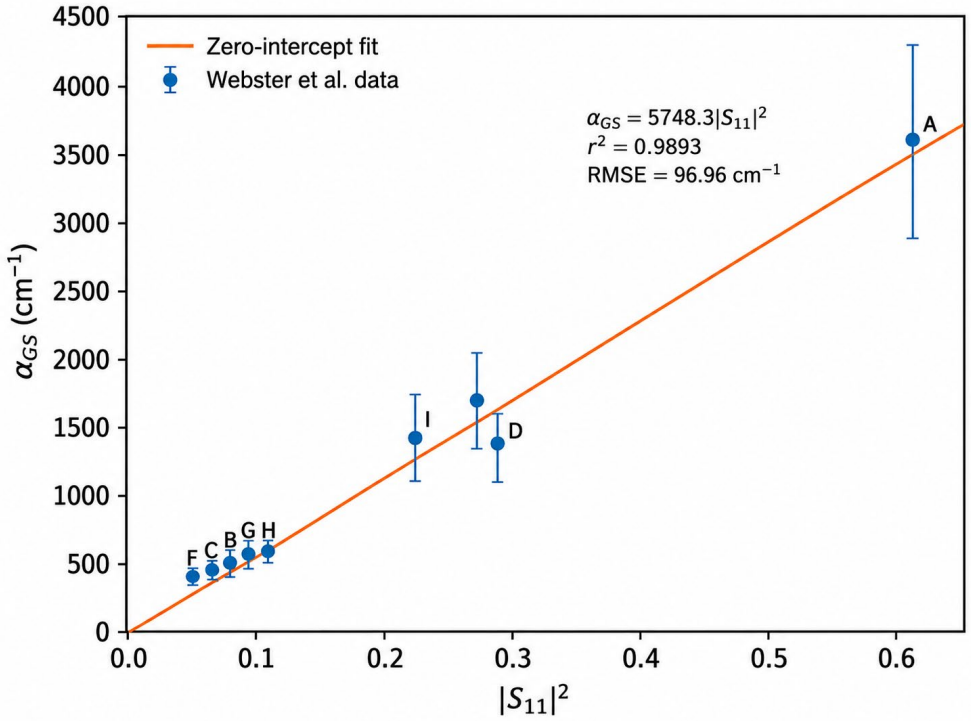

Figure 8. Quantitative relationship between the measured room-temperature ground-state absorption coefficient and the calculated electron–heavy-hole wave-function overlap squared for the ten InAs/InAsSb type-II superlattices reported by Webster et al. The symbols and vertical error bars represent the published values and their reported $\pm\mathbf{20}\%$ absorption uncertainty, respectively. The solid line denotes the zero-intercept least-squares fit obtained in the present reanalysis.

As shown in Fig. 8, the room-temperature ground-state absorption coefficient exhibits a strong linear dependence on the electron–heavy-hole wave-function overlap squared. The zero-intercept least-squares analysis yields the relation $\alpha_{GS} = (5748.3 \pm 128.8)|S_{11}|^2$ cm^{-1}, with $r^2 = 0.9893$ and RMSE = 96.96 cm^{-1}. The fitted proportionality coefficient differs by only 0.55% from the value of 5780 ± 370 cm^{-1} reported by Webster et al. for unity wave-function overlap, confirming the reproducibility of the published overlap–absorption relationship. The largest absolute residual is obtained for sample D, for which the fitted value exceeds the measured absorption coefficient by approximately 255.5 cm^{-1}; however, this deviation remains within the reported $\pm$20% experimental uncertainty. These results quantitatively confirm that the envelope-function overlap is the dominant parameter controlling the ground-state absorption strength across the investigated InAs/InAsSb type-II superlattices.

Table 3. Note: $|S_{11}|^2$ values correspond to the 295 K data; the uncertainty column is calculated as 20% of αGS.

Webster et al. A–J samples: overlap–absorption data			
Sample	**$\|S11\|^2$**	**αGS (cm⁻¹)**	**±20% error (cm⁻¹)**
A	0.609	3571	714.2
B	0.081	456	91.2

C	0.065	455	91.0
D	0.288	1400	280.0
E	0.101	517	103.4
F	0.061	422	84.4
G	0.090	572	114.4
H	0.103	577	115.4
I	0.277	1645	329.0
J	0.235	1395	279.0

Taken together, the results presented in Figs. 5–8 provide complementary numerical and experimental validation of the proposed theoretical framework. The $\boldsymbol{q}$-resolved calculations for sample B establish a direct connection between miniband dispersion, transition-energy variation, electron–heavy-hole wave-function overlap, and the resulting absorption response. The calculated ground-state transition threshold and absorption coefficient agree reasonably well with the corresponding experimental values. In addition, the independent reanalysis of the ten InAs/InAsSb superlattices reported by Webster et al. reveals a strong linear correlation between the measured ground-state absorption coefficient and the calculated overlap squared, with $r^2 = 0.9893$. These findings demonstrate that the near-edge optical response is governed jointly by the miniband energy distribution and the spatial overlap of the electron and heavy-hole envelope functions. The broader physical implications of these results for quantum-well and superlattice optical engineering are discussed in the following section.

8. Comparative Discussion and Physical Implications.

In isolated symmetric wells, the envelope-function overlap imposes additional selection rules, with transitions between subbands of equal index being dominant in the infinite-barrier limit. Finite-barrier penetration weakens this strict condition and permits lower-intensity transitions between states of compatible symmetry.

In a periodic superlattice, the transition threshold becomes $\boldsymbol{q}$-dependent because both the electron and heavy-hole states acquire miniband dispersions. The measured response therefore represents a weighted superposition of transitions distributed over a finite energy interval, where the contribution of each state is controlled by $|S_{ij}(q)|^2$. The smoothing of the absorption edge is thus determined jointly by miniband dispersion, envelope-function overlap, and spectral broadening.

The resulting structure–response relation can be expressed as follows: the well and barrier dimensions determine carrier confinement and interwell coupling; the coupling controls the miniband widths and envelope-function localization; and these quantities determine the transition-energy distribution and optical overlap. Figure 1 summarizes this relationship schematically.

For sample B, the calculated first electron miniband extends from 21.732 to 33.289 meV, corresponding to a width of 11.558 meV, whereas the first heavy-hole miniband is practically dispersionless. Consequently, the ground-state transition energy increases from 102.181 meV at the Brillouin-zone centre to 113.739 meV at the zone boundary. Over the same interval, the overlap squared decreases from 0.1018 to nearly zero. These results show that the near-edge transition-energy dispersion is governed predominantly by the electron miniband, while the high- $\boldsymbol{q}$ optical contributions are suppressed by the decreasing electron–heavy-hole overlap.

From an application perspective, isolated quantum wells provide relatively sharp transition thresholds, whereas tunnel-coupled superlattices offer a broader and more continuously tunable near-edge response. The latter behavior is particularly relevant to type-II infrared absorbers, where layer dimensions and miniband engineering are used to adjust the spectral range [21].

The obtained results are also important from a practical standpoint. In quantum wells, the shift of the absorption edge and the step-like spectral structure may be advantageous for the development of selective photodetectors, optical modulators, and narrow-band absorbing layers. In superlattices, by contrast, the smoothing of the spectrum due to miniband dispersion and the emergence of nonzero absorption near the threshold provide advantages for designing optoelectronic devices with broader spectral sensitivity. Photoluminescence studies of n-CdS/p-CdTe heterostructures show that optical excitation strongly modifies near-band-edge, interface, and polariton emission [22]. Thus, the theoretical analysis

shows that the optical properties can be purposefully controlled through an appropriate choice of heterostructure parameters. More generally, theoretical studies of other low-dimensional semiconductor systems have shown that interband photon absorption can exhibit pronounced spectral and temperature dependences, with the optical response also being strongly influenced by light polarization [23]. Photoconductivity studies of $CdSe_xS_{1-x}$ thin films further show that the spectral optical response of semiconductor materials is strongly governed by composition and carrier excitation processes [24]. Related miniband and intermediate-band concepts are also being explored in quantum-dot superlattices for improving the efficiency of intermediate-band semiconductor solar cells, further highlighting the broader relevance of superlattice-based spectral engineering [25].

The present calculation demonstrates the sensitivity of the infrared absorption response to miniband dispersion and spatial overlap for one experimentally characterized structure. A systematic optimization of well width and barrier thickness would require recalculating the carrier spectra and envelope functions for a series of structures. Such a parametric analysis represents a natural extension of the present work.

9. Limitations and Outlook.

At the same time, the present model has certain limitations. The analysis has been carried out within the framework of the effective mass approximation and the single-particle approach, while interface imperfections, multiband coupling, internal electric fields, and excitonic corrections have not been taken into account in detail. In the low-temperature regime, excitonic effects may further modify the spectral profile near the absorption edge. Recent calculations of exciton states and interband absorption spectra in quantum wells have shown that electron–hole interaction can substantially reshape the near-threshold optical response [26]. Therefore, in future studies, incorporating excitonic effects, strain, realistic band offsets, and interface roughness into the model would bring the results into closer agreement with experimental observations. Defect-related effects may also need to be considered in realistic semiconductor absorbers, since deep defect states can strongly influence photovoltage relaxation and carrier dynamics in polycrystalline optoelectronic films [28]. Future extensions may also include valence–conduction band mixing and temperature-dependent band-gap effects, which have been shown to influence interband single-photon absorption in semiconductor systems [29]. More refined models may also include position-dependent effective mass and semi-confined effects, which have recently been shown to influence the calculated optical properties of GaAs quantum wells [30].

In the present work, however, the analysis is restricted to single-particle interband transitions, so that the role of miniband dispersion can be isolated more transparently.

10. Conclusion

A common effective-mass and envelope-wave-function framework has been developed for the analysis of carrier states and interband optical absorption in isolated quantum wells and periodic superlattices. The formulation combines finite-barrier quantization, transfer-matrix miniband calculations, the optical joint density of states, and electron–hole envelope-function overlap within a consistent single-particle model. This approach enables the effects of confinement, barrier penetration, and interwell coupling on the optical response to be evaluated on the same theoretical basis.

For the InAs/InAsSb type-II superlattice corresponding to sample B, the calculated ground-state transition energy varies from 102.181 to 113.739 meV across the first Brillouin zone, while the electron–heavy-hole envelope-function overlap squared decreases from 0.1018 to nearly zero. The calculated absorption threshold of 102.181 meV differs from the experimentally reported onset of 103 meV by approximately 0.82 meV. The structural and band-edge parameters used in this calculation were derived from the spectroscopic-ellipsometry and photoluminescence data reported in Ref. [27], whereas the calculated absorption plateau of $523.1 cm^{-1}$ shows reasonable agreement with the room-temperature experimental value of $456 cm^{-1}$ reported in Ref. [18]. The reanalysis of the published A–J sample data further confirms a strong relationship between the ground-state absorption coefficient and the squared electron–heavy-hole overlap.

These results demonstrate that the near-edge infrared response of a type-II superlattice is governed jointly by the miniband transition-energy distribution and the spatial overlap of the electron and heavy-hole envelope functions. This interpretation is consistent with recent studies showing that miniband engineering

plays a central role in determining the optical absorption and device-relevant characteristics of type-II superlattice absorbers [21]. The proposed framework may therefore serve as a physically transparent first-order tool for analysing quantum-confined infrared absorbers and related optoelectronic heterostructures.

The present formulation is restricted to single-particle interband transitions. Further development of the model should include strain, band nonparabolicity, multiband coupling, excitonic effects, interface roughness, alloy disorder, and internal electric fields. The incorporation of interband multiphoton processes and field-dependent optical interactions may additionally extend the model to high-field and nonlinear semiconductor optics [31].

Acknowledgments

The authors sincerely thank **Prof. Rasulov Rustam Yavkachovich, Professor of the Department of Physics at Fergana State University**, for his valuable scientific guidance, helpful suggestions, and constructive discussions.

Conflict of Interest

The authors declare no conflict of interest.

REFERENCES

[1]. Yusupov, F. T., Rakhmonov, T. I., Akhmadjonov, M. F., Madrahimov, M. M., & Abdullayev, S. S. (2024). Enhancing ZnO/Si heterojunction solar cells: A combined experimental and simulation approach. East European Journal of Physics, 2024(3), 425–434. https://doi.org/10.26565/2312-4334-2024-3-51

[2]. Hong, S.-C., Kothiyal, G. P., Singh, J., Bhattacharya, P. K., Cunningham, J. E., Jan, W. Y., Miller, D. A. B., & Chemla, D. S. (1988). Theoretical and experimental studies of optical absorption in strained quantum-well structures for optical modulators. Physical Review B, 37(2), 878–885. https://doi.org/10.1103/PhysRevB.37.878

[3]. Ben Nasr, A., Habchi, M. M., Bilel, C., Rebey, A., & El Jani, B. (2015). Theoretical calculations of absorption spectra of GaNAsBi-based MQWs operating at 1.55 μm. Journal of Alloys and Compounds, 647, 159–166. https://doi.org/10.1016/j.jallcom.2015.06.105

[4]. Leenaerts, O., Vercauteren, S., Schoeters, B., & Partoens, B. (2016). System-size dependent band alignment in lateral two-dimensional heterostructures. 2D Materials, 3(2), 025012. https://doi.org/10.1088/2053-1583/3/2/025012

[5]. Ploog, K. (1986). Artificial Semiconductor Superlattices and Quantum Well Structures. Europhysics News, 17(4), 44–47. https://doi.org/10.1051/epn/19861704044

[6]. Schmitt-Rink, S., Chemla, D. S., & Miller, D. A. B. (1989). Linear and nonlinear optical properties of semiconductor quantum wells. Advances in Physics, 38(2), 89–188. https://doi.org/10.1080/00018738900101102

[7]. LEFEBVRE, P., CHRISTOL, P., & MATHIEU, H. (1993). General formalism for excitonic absorption edges in confined systems with arbitrary dimensionality. Le Journal de Physique IV, 03(C5), 377–380. https://doi.org/10.1051/jp4:1993579

[8]. Yahyaoui, N., Hammouda, K., Zeiri, N., Said, M., Ali, M. E. E. S., Hendi, A. S. A., & Duque, C. A. (2025). Impact of the applied electric field on the optical absorption coefficient in Ge/Si_{1-x}Ge_{x} step quantum well (SQW). Discover Applied Sciences, 7, Article 403. https://doi.org/10.1007/s42452-025-06685-z

[9]. Burt, M. G. (1992). The justification for applying the effective-mass approximation to microstructures. Journal of Physics: Condensed Matter, 4(32), 6651–6690. https://doi.org/10.1088/0953-8984/4/32/003

[10]. BenDaniel, D. J., & Duke, C. B. (1966). Space-charge effects on electron tunneling. Physical Review, 152(2), 683–692. https://doi.org/10.1103/PhysRev.152.683

[11]. Bastard, G. (1981). Superlattice band structure in the envelope-function approximation. Physical Review B, 24(10), 5693–5697. https://doi.org/10.1103/PhysRevB.24.5693

[12]. Bastard, G. (1982). Theoretical investigations of superlattice band structure in the envelope-function approximation. Physical Review B, 25(12), 7584–7597. https://doi.org/10.1103/PhysRevB.25.7584

[13]. Rasulov, R. Y., Rasulov, V. R., Mamatova, M. A., & Nasirov, M. K. (2024). Theory of electron transport in two-barrier five-layer semiconductor structures. East European Journal of Physics, 3, 310–315. https://doi.org/10.26565/2312-4334-2024-3-33

[14]. Fang, S., Hao, R., Zhang, L., Guo, J., & Liu, W. (2022). Simulation of the band structure of InAs/GaSb type II superlattices utilizing multiple energy band theories. Frontiers in Physics, 10, Article 822800. https://doi.org/10.3389/fphy.2022.822800

[15]. Esaki, L., & Tsu, R. (1970). Superlattice and negative differential conductivity in semiconductors. IBM Journal of Research and Development, 14(1), 61–65. https://doi.org/10.1147/rd.141.0061

[16]. Gu, Z., Zhu, Z. N., Wang, M. M., Wang, Y. Q., Cui, H. L., & Ban, S. L. (2017). Interband optical absorption in wurtzite MgxZn1−xO/ZnO/MgyZn1−yO asymmetric quantum wells. Superlattices and Microstructures, 102, 391–398. https://doi.org/10.1016/j.spmi.2016.12.032

[17]. Spector, H. N. (1983). Free-carrier absorption in quasi-two-dimensional semiconducting structures. Physical Review B, 28(2), 971–976. https://doi.org/10.1103/physrevb.28.971

[18]. Webster, P. T., Riordan, N. A., Liu, S., Steenbergen, E. H., Synowicki, R. A., Zhang, Y.-H., & Johnson, S. R. (2015). Absorption properties of type-II InAs/InAsSb superlattices measured by spectroscopic ellipsometry. Applied Physics Letters, 106(6), 061907. https://doi.org/10.1063/1.4908255

[19]. Satzke, K., Weiser, G., Stolz, W., & Ploog, K. (1991). Absorption and electroabsorption spectra of (In,Ga)As/(In,Al)As quantum wells and superlattices, grown lattice matched to InP substrates. Physical Review B, 43(3), 2263–2272. https://doi.org/10.1103/PhysRevB.43.2263

[20]. Helm, M., Hilber, W., Fromherz, T., Peeters, F. M., Alavi, K., & Pathak, R. N. (1993). Infrared absorption in superlattices: A probe of the miniband dispersion and the structure of the impurity band. Physical Review B, 48(3), 1601–1610. https://doi.org/10.1103/PhysRevB.48.1601

[21]. Singh, A., & Muralidharan, B. (2024). Insights into optical absorption and dark currents of the 6.1 Å type-II superlattice absorbers for MWIR and SWIR applications. Journal of Applied Physics, 136(5), 055703. https://doi.org/10.1063/5.0218463

[22]. Polvonov, B. Z., Gafurov, Y. I., Otajonov, U. A., Nasirov, M. X., & Zaylobiddinov, B. B. (2023). The specificity of photoluminescence n-CdS/p-CdTe in semiconductor heterostructures. *International Journal of Mathematics and Physics, 13*(2), 12–19. https://doi.org/10.26577/ijmph.2022.v13.i2.02

[23]. Rasulov, R. Y., Rasulov, V. R., Nasirov, M. K., Kuchkarov, M. K., & Urinova, K. K. (2025). Spectral and temperature dynamics of photon absorption in monatomic transition metal dichalcogenides. *East European Journal of Physics*, **2**, 231–236. https://doi.org/10.26565/2312-4334-2025-2-26

[24]. Akhmadaliyev, B., Rakhmonov, T., Sulaimonov, K., & Nurmatov, O. (2024). Photoconductivity spectra of thin solid solution films $CdSe_xS_{1-x}$. E3S Web of Conferences, 583, Article 04002. https://doi.org/10.1051/e3sconf/202458304002

[25]. Petrosyan, N., Yeganyan, L., Manaselyan, A., Mughnetsyan, V., Gudmundsson, V., & Kirakosyan, A. (2026). Enhanced efficiency of intermediate-band semiconductor solar cells embedded with quantum dot superlattices. Physics Letters A, 584, 131639. https://doi.org/10.1016/j.physleta.2026.131639

[26]. Wu, S. (2025). Exciton states and interband absorption spectra in quantum wells using a variationally optimized diagonalization method. The European Physical Journal B, 98, Article 1. https://doi.org/10.1140/epjb/s10051-024-00854-6

[27]. Webster, P. T., Riordan, N. A., Liu, S., Steenbergen, E. H., Synowicki, R. A., Zhang, Y.-H., & Johnson, S. R. (2015). Measurement of InAsSb bandgap energy and InAs/InAsSb band edge positions using spectroscopic ellipsometry and photoluminescence spectroscopy. *Journal of Applied Physics, 118*(24), 245706. https://doi.org/10.1063/1.4939293

[28]. Nurmatov, O., Tolaboyev, D., Akhmadjonov, M., Abdubannobov, M., Akhmadaliyev, J., Qodirov, X., Tursunov, I., & Yulchiev, I. (2026). Role of deep defect states in anomalous photovoltage relaxation of polycrystalline silver-doped cadmium telluride thin films. Informacije MIDEM: Journal of Microelectronics, Electronic Components and Materials, 56(1). https://doi.org/10.33180/InfMIDEM2026.105

[29]. Rasulov, R. Y., Rasulov, V. R., Kodirov, N. U., Nasirov, M. K., & Eshboltaev, I. M. (2025). Theoretical analysis of interband single-photon light absorption in semiconductors: Effects of valence-conduction band mixing and temperature-dependent bandgap. East European Journal of Physics, 2, 179–187. https://doi.org/10.26565/2312-4334-2025-2-18

[30]. Al, E. B., Jafarov, E. I., Jafarova, A. M., & Ungan, F. (2026). Theoretical investigation of optical properties in GaAs quantum wells under position-dependent mass and semi-confined effects. Physics Letters A, 582, Article 131572. https://doi.org/10.1016/j.physleta.2026.131572

[31]. Rustam Y. Rasulov, Vokhob R. Rasulov, Forrukh U. Kasimov, Mardonbek Kh. Nasirov, Islam E. Farmanov, On the theory of interband two-photon absorption of light in semiconductors accounting admixtures to the states of the conduction band and valence states, the Rabi effect, East European Journal of Physics 2 (2025) 200–205. https://doi.org/10.26565/2312-4334-2025-2-20

Arrived: 01.05.2026
Accepted: 31.07.2026